VRIJE
UNIVERSITEIT
BRUSSEL

Thesis submitted in order to achieve the degree of master in Physics and Astronomy

BACKGROUND MEASUREMENTS FOR THE MILLIQAN EXPERIMENT

Yens Elskens

June 5, 2020

Prof. dr. Steven Lowette

Science & Bio-engineering Sciences

Abstract

A new scintillator-based LHC experiment called milliQan, which is designed to detect particles with a non-integer charge, is introduced. This experiment will be placed near interaction point 5 of the LHC. Background measurements have been performed using a $1\,\%$ demonstrator, placed at the foreseen experimental cavern for the full detector. We consider two main types of background: the internal background, which consists of any radiation coming from the used material itself, and the external background, which consists mostly of cosmic radiation. The internal background appears to play a very important role and this should be taken into account when designing and operating the eventual experiment. The angular distribution of the external background was found to be not significantly influenced by the presence of large vertical access shafts near Point 5. All the experiments needed to gain these results have been assembled and were conducted by the author of this thesis and were supervised by prof. dr. Steven Lowette and/or members of the milliQan collaboration.

Deze masterproef is (ten dele) tot stand gekomen in de periode dat het hoger onderwijs onderhevig was aan een lockdown en beschermende maatregelen ter voorkoming van de verspreiding van het COVID-19 virus. Het proces van opmaak, de verzameling van gegevens, de onderzoeksmethode en/of andere wetenschappelijke werkzaamheden die ermee gepaard gaan, zijn niet altijd op gebruikelijke wijze kunnen verlopen. De lezer dient met deze context rekening te houden bij het lezen van deze masterproef, en eventueel ook indien sommige conclusies zouden worden overgenomen.

This master's thesis came about (in part) during the period in which higher education was subjected to a lockdown and protective measures to prevent the spread of the COVID-19 virus. The process of formatting, data collection, the research method and/or other scientific work the thesis involved could therefore not always be carried out in the usual manner. The reader should bear this context in mind when reading this Master's thesis, and also in the event that some conclusions are taken on board.

Contents

Introduction

Over the last century, particle physics has undergone a revolution. New scientific discoveries and technological development have pushed each other to their limits and beyond. As a result, we now have a beautiful, elegant and (most importantly) testable model which describes the known elementary particles and their interactions, namely the Standard Model (SM) of particle physics.

Since its founding, the European Organization for Nuclear Research (CERN) has played a vital role in this revolution at an ever accelerating rate. Now more than ever, CERN has been securing its position at the frontiers of particle physics research, holding now for a decade the Large Hadron Collider (LHC), the sole accelerator allowing us to test the SM at the highest energies, and to search for new physics, using proton collisions at a record collision energy of $13\,\mathrm{TeV}$.

One of the main challenges of this time is the search for Dark Matter. All experiments to date have failed to identify this Dark Matter, much less measure its properties. Although many theories have been proposed to explain this ubiquitous invisible matter, one direction which many physicists are exploring is the possibility that Dark Matter consists of a collection of particles which are not charged directly under any of the Standard Model interactions, which is usually referred to as a hidden or dark sector. Depending on the symmetry and contents of such a hidden sector, the production of particles with a non-integer (or fractional) electric charge is possible. Such particles are very interesting from an experimental point of view as they can serve as a portal to probe a possible hidden sector.

This thesis will introduce a new future LHC experiment called *milliQan* which is specifically designed to detect fractionally charged particles. The focus will lie on background studies we conducted at the experimental site. We distinguish two main types of background: on the one hand any influence coming from within the used material (or *internal background*), on the other hand the *external background* which consists mostly of cosmic radiation or any radiation present in the experimental cavern. While the internal background will be examined on relevance, the angular distribution of the external background will be ascertained on symmetry.

This thesis has been constructed in five chapters. Chapter 1 briefly introduces

the Standard Model and the principle of hidden sectors and provides both theoretical as experimental motivations for the search to fractionally charged particles. In chapter 2 the LHC and its aspects relevant for our analyses are discussed and the milliQan experiment is introduced. These analyses are exemplified in chapters 3 and 4 which respectively study the internal and external backgrounds. A conclusion and outlook is provided in chapter 5.

It should be noted that all the mentioned background experiments were assembled and conducted in the experimental milliQan cavern at CERN by the author of this thesis and were supervised by prof. dr. Steven Lowette and/or members of the milliQan collaboration.

Chapter 1

Motivation

1.1 Theoretical Motivation

1.1.1 The Standard Model

The Standard Model (SM) of particle physics is a quantum field theory that describes elementary particles and their fundamental interactions. It is a mathematical construction supplemented by experimentally determined parameters. A first classification of elementary particles is made based on their quantum mechanical spin (as can be seen in Figure 1.1): one distinguishes fermions (spin-$\frac{1}{2}$ particles), gauge bosons or *force mediators* (spin-1 particles) and the Brout-Englert-Higgs boson (spin-0 particle).
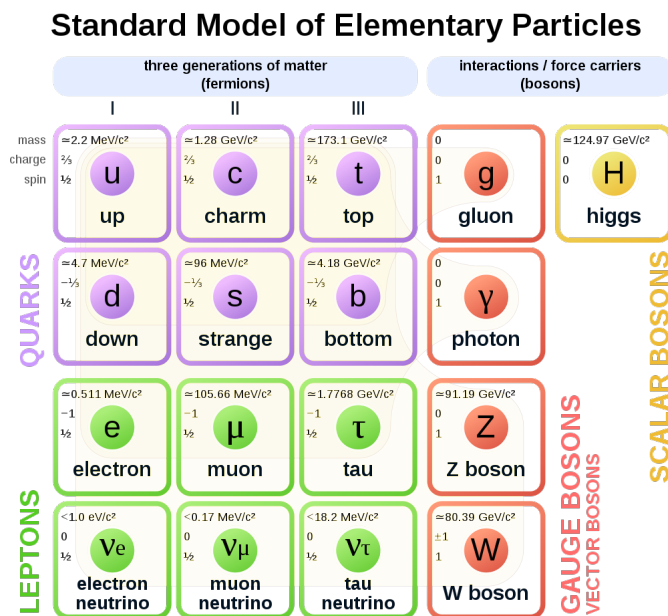

Figure 1.1: Schematic view of the Standard Model. [1]

The construction of the SM is based on symmetries motivated by gauge invariance. The relevant symmetry groups are

$$SU(3)_{\text{QCD}} \times SU(2)_L \times U(1)_Y .$$

The $SU(3)$ symmetry describes the strong interaction (mediated by eight gluons) between particles carrying colour charge: the quarks (top left corner in Figure 1.1). Each quark can be assigned one of six flavours (u, d, c, s, t or b) and one of three colours: *red* (r), *green* (g) or *blue* (b). Therefore this gauge theory is known as *Quantum Chromodynamics* (QCD).

The photon (describing the electromagnetic force) and the Z^0- and $W^\pm$ bosons (describing the weak force) result from the chiral $SU(2)_L \times U(1)_Y$ symmetry. The $SU(2)$ group describes doublets of left-handed chiral particle states [2]

$$\Psi^L = \begin{pmatrix} \ell^L \\ \nu_\ell^L \end{pmatrix} ,$$

where ℓ runs over the lepton flavours $\ell \in \{e, \mu, \tau\}$. This symmetry generates three electrically neutral fields: W_μ^1, W_μ^2 and W_μ^3. The $U(1)$ group describes singlets of right-handed leptons (right-handed neutrinos have not been experimentally observed) and generates one field B_μ with coupling the hypercharge Y (hence the 'Y' in the subscript). In order to describe weak interactions without violating conservation of electric charge, an electrically charged boson is required. Therefore the charged $W^\pm$ gauge field (coupling solely to left-handed chiral particle states) is defined as a linear combination of two of the three $SU(2)_L$-fields [2]

$$W_\mu^\pm = \frac{1}{\sqrt{2}} \left(W_\mu^1 \mp i W_\mu^2 \right) . \tag{1.1}$$

The neutral Z-boson field and photon field are now written as a rotation of the W_μ^3 and B_μ fields over the so-called *weak mixing angle* θ_W [3]

$$\begin{pmatrix} Z_\mu \\ A_\mu \end{pmatrix} = \begin{pmatrix} \cos\theta_W & -\sin\theta_W \\ \sin\theta_W & \cos\theta_W \end{pmatrix} \begin{pmatrix} W_\mu^3 \\ B_\mu \end{pmatrix} . \tag{1.2}$$

By adding a scalar $SU(2)$-doublet to the standard model which acquires a nonzero vacuum expectation value, masses for the Z and W-bosons (as well as fermion masses, through Yukawa coulpings) can be generated through the Brout-Englert-Higgs (BEH) mechanism by adding a massive scalar boson (top right corner in Figure 1.1) and having a nonzero vacuum expectation value for its corresponding field. This mechanism spontaneously breaks the $SU(2)_L \times U(1)_Y$ symmetry to a $U(1)_{\text{EM}}$ symmetry.

1.1.2   Beyond the Standard Model

How elegant the Standard Model may be, it is not the end of the road. There are still both experimental motivations (like Dark Matter, neutrino oscillations

... as well as certain experimental anomalies) and theoretical indications (like the hierarchy problem, the strong CP problem...) for extending the Standard Model with new physics. A very general way to look for new physics from a theoretical perspective is by hypothesizing the existence of one or multiple new particles which are not charged directly under strong, weak or electromagnetic interactions. Such a collection of particles is usually referred to as a *hidden sector* or *dark sector* and can be introduced by adding an extra gauge symmetry, G', to the Standard Model's $SU(3)_{QCD} \times SU(2)_L \times U(1)_Y$ symmetry. From an experimental point of view, it is of course vital that the content of such a hidden sector could interact through some mechanism with the SM particles. Therefore, hidden sector theories usually include one or more mediator particles coupled to the SM through a so-called *portal*. Such mediator particles which allow for renormalizable portals can be vectors, scalars or fermions interacting with the SM through a vector, Higgs, or neutrino portal respectively [4].

The symmetry and contents of such a hidden sector are, of course, dependent on the physics phenomena that are trying to be described or explained. Even though extended gauge groups are very general and have a very broad applicability, their use has become very popular over the last decade within Dark Matter research. Here, an Abelian $U(1)'$ extension to the electroweak $SU(2)_L \times U(1)_Y$ gauge symmetry is considered, interacting with the SM through a vector portal. Such a portal exists of a kinetic mixing operator between the SM hypercharge field and the Abelian $U(1)'$ vector field.

Extended Abelian Gauge Groups & Kinetic Mixing

We consider a single additional $U(1)'$ factor, with initially no kinetic mixing. If the corresponding gauge field is denoted Z_2^0, and (initially) no kinetic mixing is inflicted, the Lagrangian for the SM coupling of three neutral currents can be written as [5]

$$\mathcal{L} = -g J_3^\mu W_\mu^3 - g_Y J_Y^\mu B_\mu - g_2 J_2^\mu Z_{2\mu}^0 \tag{1.3a}$$

$$= -e J_{EM}^\mu A_\mu - g_1 J_1^\mu Z_{1\mu}^0 - g_2 J_2^\mu Z_{2\mu}^0 \tag{1.3b}$$

where A_μ and $Z_{1\mu}^0$ are the SM photon and Z-boson field respectively and the currents $J_{1,2}^\mu$ are defined as [5]

$$J_\alpha^\mu = \sum_r \bar{\psi}_r \gamma^\mu \left[\epsilon_L^\alpha(r) P_L + \epsilon_R^\alpha P_R \right] \psi_r = \frac{1}{2} \sum_r \bar{\psi}_r \gamma^\mu \left[g_V^\alpha(r) - g_A^\alpha(r) \gamma^5 \right] \psi_r . \tag{1.4}$$

Considering the case of one or multiple complex scalar fields ϕ_i, it is possible for some of those scalars to acquire vacuum expectation values and thus generate masses for the gauge bosons. A mass-squared matrix can then be developed for the two Z-fields

$$M_{Z-Z'}^2 = \begin{pmatrix} M_{Z^0}^2 & \Delta^2 \\ \Delta^2 & M_{Z'}^2 \end{pmatrix} , \tag{1.5}$$

which can be diagonalized using the following expression for the mass eigenstates [5]

$$\begin{pmatrix} Z_1 \\ Z_2 \end{pmatrix} = \begin{pmatrix} \cos\theta & \sin\theta \\ -\sin\theta & \cos\theta \end{pmatrix} \begin{pmatrix} Z_1^0 \\ Z_2^0 \end{pmatrix} , \tag{1.6}$$

with corresponding eigenvalues [5]

$$M_{1,2}^2 = \frac{1}{2}\left[M_{Z^0}^2 + M_{Z'}^2 \mp \sqrt{\left(M_{Z^0}^2 - M_{Z'}^2\right)^2 + 4\Delta^4} \right] . \tag{1.7}$$

The mixing angle is then given by [5]

$$\theta = -\frac{1}{2}\arctan\left(\frac{2\Delta^2}{M_{Z'}^2 - M_{Z^0}^2}\right) . \tag{1.8}$$

When considering an Abelian gauge symmetry, not only the mixing of mass eigenstates but also kinetic mixing is allowed. As mentioned earlier, a kinetic mixing operator will act as a vector portal to the SM. When looking at the case after spontaneous symmetry breaking (thus with the remaining $U(1)_{\text{EM}} \times U(1)'$ gauge symmetry), the most general kinetic mixing term that can be written down is [5]

$$\mathcal{L}_{\text{kin}} = -\frac{c_1}{4}F_{\mu\nu}F^{\mu\nu} - \frac{c_2}{4}F'_{\mu\nu}F'^{\mu\nu} - \frac{c_{12}}{4}F_{\mu\nu}F'^{\mu\nu} \tag{1.9}$$

where $F_{\mu\nu}$ and $F'_{\mu\nu}$ are the electromagnetic and dark Z field strength tensors respectively. It is worth mentioning that so far everything has been kept very general: no constraints on the Z'-mass or the kinetic mixing coupling strength have been implemented, which leaves quite some freedom for different models describing new physics. In the next paragraph a more specific model is described, which gives rise to the existence of long-lived particles with a charge much smaller than the elementary charge.

Fractionally Charged Particles

Considering the gauge boson A'_μ associated to a hidden sector $U(1)'$ gauge symmetry to be massless and having the ability to couple to a hidden sector massive Dirac fermion ψ with mass M_ψ, the Lagrangian can be written as

$$\mathcal{L} = \mathcal{L}_{\text{SM}} - \frac{1}{4}F'_{\mu\nu}F'^{\mu\nu} + i\bar{\psi}\left(\slashed{\partial} + ie'\slashed{A}' + iM_\psi\right)\psi - \frac{\kappa}{2}F'_{\mu\nu}B^{\mu\nu} , \tag{1.10}$$

where the kinetic mixing term has been written down before electroweak symmetry breaking such that the field strength tensors are written as

$$F'_{\mu\nu} = \partial_\mu A'_\nu - \partial_\nu A'_\mu \tag{1.11a}$$
$$B_{\mu\nu} = \partial_\mu B_\nu - \partial_\nu B_\mu \tag{1.11b}$$

with B_μ the hypercharge field. In such a case, the hidden sector gauge boson is usually referred to as the *dark photon*. The kinetic mixing term in equation (1.10) can be eliminated by redefining the dark photon field as

$$A'_\mu \to A'_\mu - \kappa B_\mu .$$

The Lagrangian now becomes

$$\mathcal{L} = \mathcal{L}_{\mathrm{SM}} - \frac{1}{4} F'_{\mu\nu} F'^{\mu\nu} + i\bar{\psi} \left(\slashed{\partial} + ie'\slashed{A}' - i\kappa e'\slashed{B} + iM_\psi \right) \psi \,, \qquad (1.12)$$

from which it is clear that the dark fermion couples to the SM hypercharge field with coupling $\kappa e'$. After electroweak symmetry breaking the dark fermion will couple to the SM photon field with coupling $\kappa e' \cos\theta_W$, thus assigning it a fractional charge. A Feynman diagram which represents how this dark photon field can be generated through, for example, $q\bar{q}$ annihilation by kinetic mixing with the weak hypercharge field, is given in Figure 1.2.

From an experimental point of view, this result is very interesting. Since electromagnetic interactions can be directly measured, particles with a fractional charge can be used to probe a possible dark sector experimentally.
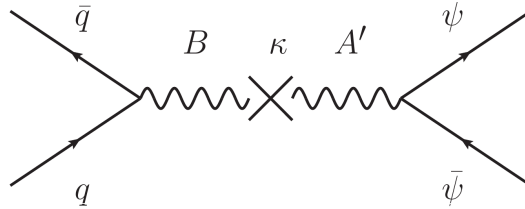

Figure 1.2: Feynman diagram of fractionally charged particle creation through kinetic mixing of the hypercharge field strength with the dark sector field strength [6].

1.2   Fractionally Charged Particle Searches

In the previous section it became clear that fractionally charged particles (FCPs) are very coveted, as they could be used to probe a possible hidden sector when coupled to a massless Abelian gauge boson. Particles with such a charge have been looked for in the past and limits on the mass for possible charges have been determined. The results of these searches are represented in Figure 1.3, which shows the excluded regions in the charge-mass plane of the dark fermion ψ. On this plot, the electromagnetic charge is given as a fraction ϵ of the electron charge e [6].

Reviewing these limits, it can be seen that at low masses the main constraints come from collider experiments before the LHC-era (the green area). These exclude the existence of particles with charge $\frac{2}{3}e$ at masses below $84\,\mathrm{GeV}$ [7]. At higher masses, the most stringent indirect limits are given by the CMB anisotropy and the requirements on the relic abundance of the low-charge particles [6]. An intriguing aspect here, is the gap in the phase space where $0.1\,e \lesssim \epsilon \lesssim 0.001\,e$ (particles with a so-called millicharge) and $0.1\,\mathrm{GeV} \lesssim M_\psi \lesssim 100\,\mathrm{GeV}$. This area, which is adjacent to the current limits set by colliders, could be interesting to cover with the LHC.
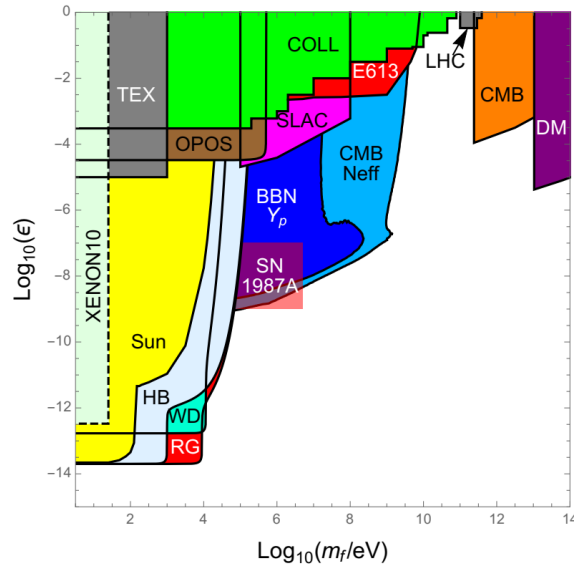
Figure 1.3: Constraints on the existence of fractionally particles in the charge-mass plane. The parameter ϵ represents the charge of the dark fermion in units of elementary charges [8].

From Figure 1.2 it was clear that $q\bar{q}$ annihilation can lead to the creation of particles with a fractional charge. This can happen through a variety of channels. The expected cross section for each of these channels (multiplied by the corresponding branching ratio and normalized by Q^2) in function of the mass of the millicharged particle is given in Figure 1.4. Comparing this figure with the yet uncovered part of the phase space in Figure 1.3, it is clear the most relevant fractionally charged particle production channel for particle colliders is through the Drell-Yan process via off-shell photons, Z bosons, J/ψ and Υ particles. A schematic diagram for this process is given in Figure 1.5.
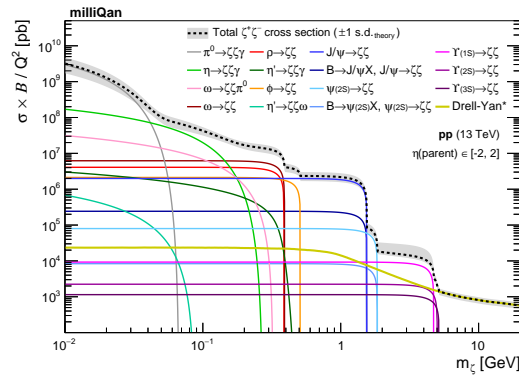

Figure 1.4: Expected cross section of decays to fractionally charged particles (here denoted as ζ) multiplied by the branching ratio, normalized by the coupling squared [9].
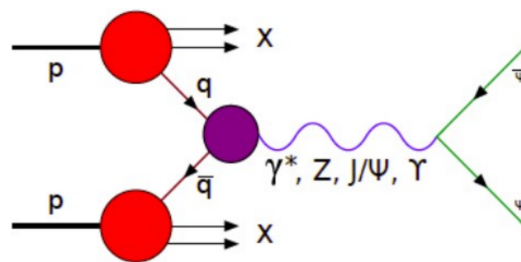
Figure 1.5: Production of fractionally charged particles from proton-proton collisions through the Drell-Yan process [10].

Chapter 2

The Large Hadron Collider & milliQan

2.1 The Large Hadron Collider

For over ten years now, CERN holds one of the most prestigious tools in experimental particle physics research: the Large Hadron Collider (LHC). The LHC is the largest and most powerful accelerator in the world to date and consists of a 27 kilometer ring instrumented with superconducting magnetic dipoles and quadrupoles [11]. It accelerates protons in two opposite directions and collides them at a center-of-mass energy of 13 TeV.
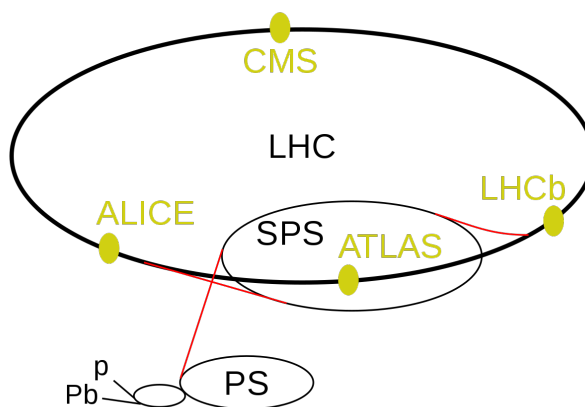
Figure 2.1: Schematic view of the LHC and its pre-accelerators [12].

Before reaching this energy, the protons have to go through a series of CERN's previous accelerators. A schematic view of this accelerator complex is depicted in Figure 2.1. All protons start from a single hydrogen bottle. From this bottle, the protons are stripped from their hydrogen atoms and are accelerated linearly up to an energy of 50 MeV through a system of cylindrical conductors which

are alternately charged positive or negative [13]. This linear accelerator is called *LINAC2* and, in order to achieve higher intensities, it will be replaced by *LINAC4* for the next restart of the LHC. After this linear acceleration, the protons enter the *proton synchrotron booster* which is composed of four superimposed synchrotron rings which accelerate the protons to an energy of 1.4 GeV before injecting them in the *proton synchrotron* (PS) [14]. Here, they reach a maximum energy of 25 GeV when they get delivered to the PS's successor: the *super proton synchrotron* (SPS). In this last step before entering the LHC, the protons reach an energy of 450 GeV [15]. Then, they get injected in two opposite directions in the LHC where each proton beam will arrive at an energy of 6.5 TeV before colliding at one of four interaction points.

Around those interaction points detectors have been placed, each designed for their own purpose. There are two general-purpose detectors: *CMS* (Compact Muon Solenoid) and *ATLAS* (A Toroidal LHC ApparatuS). They both have a very broad physics programme ranging from studying the SM to searching for extra dimensions and particles that could make up Dark Matter [16]. The *LHCb* experiment, on the other hand, studies b quarks to investigate the matter-antimatter asymmetry in the Universe [17]. Then there is still *ALICE* (A Large Ion Collider Experiment), which is a heavy ion detector designed to study the physics of strongly interacting matter at extreme energy densities.

Regardless the experiment one is working on, one piece of information that is very relevant to anyone studying LHC collisions is knowing what kind of events can be expected at the LHC and how often they can be expected to happen. This information can be achieved by introducing the *instantaneous luminosity* $\mathcal{L}$, which is a measure of the number of collisions an accelerator produces per second. For a given process $pp \to X$ it relates the rate of the produced events $\frac{\mathrm{d}N}{\mathrm{d}t}$ to its cross section $\sigma(pp \to X)$ [6]

$$\frac{\mathrm{d}N}{\mathrm{d}t} = \mathcal{L} \cdot \sigma(pp \to X) \,. \tag{2.1}$$

The instantaneous luminosity depends on a number of accelerator-specific variables and is given by [6]

$$\mathcal{L} = \frac{N_b^2 n_b f_{\mathrm{rev}} \gamma}{4\pi \epsilon_n \beta^*} F \,, \tag{2.2}$$

where N_b represents the number of protons per bunch, n_b the number of bunches per beam, f_{rev} the revolution frequency, γ is simply the Lorentz factor, ϵ_n is called the *normalized transverse beam emittance* which describes the beam spread in the position momentum phase-space and β^* represents the beta function at the interaction point. The beta function $\beta(s)$ is a measure of the transverse beam size at each point s. Since the particle bunches get focused and defocused by magnetic dipoles and quadrupoles [18], the transverse beam size does not remain constant, but instead increases and decreases, following an oscillatory motion. Finally, the factor F is a luminosity reduction factor

to account for the nonzero crossing angle between the beams [6]. The reason why the beams are collided under a nonzero angle is to prevent encounters in the region where the two beams share the same vacuum chamber [19].

In 2016 (the first year of Run 2) the luminosity peaked at a value of $1.5 \cdot 10^{34}\,\mathrm{Hz\,cm^{-2}}$. By the end of 2018, the luminosity had peaked that year at $2.1 \cdot 10^{34}\,\mathrm{Hz\,cm^{-2}}$ [20].

Figure 2.2 shows for different particle productions the expected cross section in function of their mass as well as the number of expected events per year. Here it is clear that, generally speaking, the processes of interest (like the Higgs decays, SUSY, etc.) have a very low cross section compared to the SM processes and as such have a relatively low production rate compared to the total interaction rate.
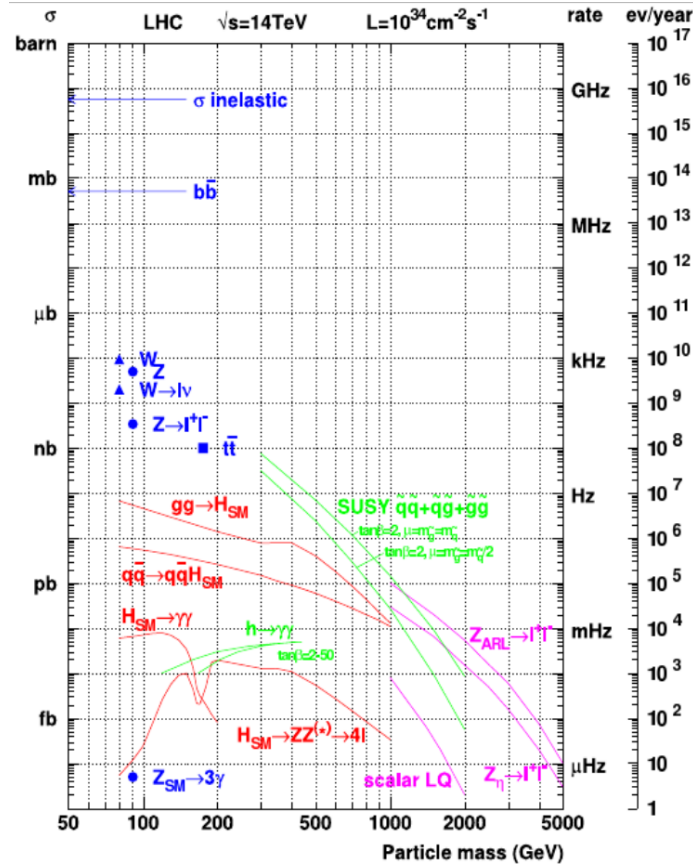

Figure 2.2: Cross section and expected number of events per year in function of the mass of the produced particle [21].

When revisiting the last paragraph of the previous chapter, it can be inferred from Figure 1.4 that the expected cross section for the most relevant FCP production channel above FCP masses of $5\,\mathrm{GeV}$ for the LHC at 13 TeV center-of-mass energy (namely through the Drell-Yan process via off-shell photons or Z bosons), is around $1\,\mathrm{nb}\,(10^{-33}\,\mathrm{cm^2})$. When comparing this to Figure 2.2,

it can be seen that the most important backgrounds for FCP searches are $Z \to \ell\ell$, $W \to \ell\nu_\ell$ and the $t\bar{t}$ production in the case where at least one of the two top quarks decays leptonically. Also leptonic decays from $b\bar{b}$-production form a very relevant background. When looking for FCPs with the LHC, it is thus important to do it in such a way that these backgrounds can be easily distinguished from the FCP signal.

2.2   milliQan

In section 1.2, when discussing the existing limits on fractionally charged particles, it was concluded that a large part of the charge-mass plane has, so far, still been left uncovered. For standard LHC experiments, like CMS, detecting very low-charged particles is not an easy task as the momentum p of a particle is proportional to the inverse of its charge: $p \sim \frac{1}{Q}$ and, according to the Bethe-Bloch formula, the ionization energy loss of a particle $\frac{\mathrm{d}E}{\mathrm{d}x}$ is proportional to Q^2. This indicates that such particles will advance straight through the detector without losing much energy. In order to be able to identify fractional charges we are in need of much more sensitive detection techniques, which can be obtained by adding a new experiment in a low-background area. A proposal for such a novel experiment at the LHC is *milliQan*, which will be located near the Point 5 interaction point (IP).

2.2.1   Detector Design

The proposed detector is designed to search for particles with a millicharge ($\epsilon \sim 10^{-3}\,e$, conveniently called millicharged particles or mCPs) such that it would allow us to cover part of the "gap" in the mass range $1\,\mathrm{GeV} \lesssim M_\psi \lesssim 100\,\mathrm{GeV}$ in the phase space shown in Figure 1.3. This design is composed of two $1\,\mathrm{m} \times 1\,\mathrm{m} \times 3\,\mathrm{m}$ plastic scintillator arrays, next to each other [22]. These arrays should be oriented such that the long axis points towards the CMS IP. As can be seen in Figure 2.3, depicting a sketch of one of the milliQan arrays, these arrays are divided in nine "steps", stacked on top of each other. Each step contains six modules next to each other and, according to the current design, each module contains four[1] longitudinal layers. Every layer consists of four $5\,\mathrm{cm} \times 5\,\mathrm{cm} \times 60\,\mathrm{cm}$ scintillators, optically coupled to high-gain photo-multiplier tubes (PMTs), which will be referred to as "bars" [22]. There are thus a total of 864 bars per array [22]. Finally, each of these arrays is surrounded by active muon veto shields composed of six scintillator panels.

Since milliQan would be placed outside the CMS detector (see next section), the most relevant collision backgrounds are the ones containing muons, like $Z \to \mu\mu$ and $W \to \mu\nu_\mu$ processes as well as $t\bar{t}$ production where at least one of

---

[1]Originally three layers were considered, which is why only three layers are depicted in Figure 2.3. However, later on it was decided that three layers was not enough to sufficiently suppress background and a fourth layer was added to the design.
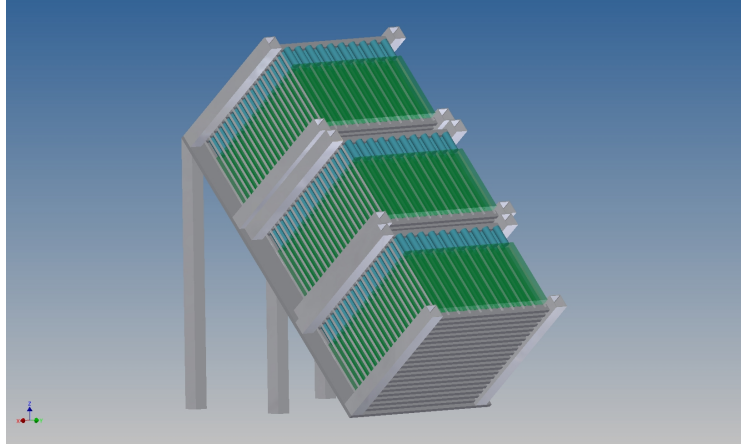
Figure 2.3: Sketch of one milliQan array of modules [22].

the two top quarks decays to a muon. Also the $b\bar{b}$ production delivers a very large rate of muons. A muon would lose roughly $2\,\mathrm{MeV\,cm^{-1}}$ of energy in a material of density $1\,\mathrm{g\,cm^{-3}}$ [23]. For a plastic scintillator, about 10^4 photons per MeV are expected to be released from such an energy deposition. Thus, for a 60 cm bar, a particle with charge e is expected to produce

$$10^4\,\mathrm{photons\,MeV^{-1}} \times 2\,\mathrm{MeV\,cm^{-1}} \times 60\,\mathrm{cm} = 1.2 \cdot 10^6\,\mathrm{photons}\,,$$

in each scintilator. Now considering particles with millicharges, recalling that the energy loss decreases by a factor of Q^2, an average of $\mathcal{O}(1)$ photo-electrons (PE) from each attached PMT is expected [24]. Therefore milliQan should be able to relatively easily distinguish muons from millicharged particles based on the number of photo-electrons expected to be created.

2.2.2   Experimental Site

As mentioned earlier, an experiment like milliQan should be placed in a low-background area. Even though milliQan should be able to easily distinguish muons from millicharged particles, the LHC muon flux should still be shielded to avoid a too large rate. On the other hand, the detector should not be placed too far from the interaction point as the mCP flux will also drop according to the inverse of the distance to the IP squared. A place which provides a good tradeoff between those two effects is the PX56 drainage gallery above the CMS experimental cavern. Using a 3D model constructed from a laser scan of the tunnel, an ideal position for milliQan was found (see Figure 2.4a). The chosen location is above the CMS experimental cavern, 33 m from the IP, positioned at an azimutal angle of $43.1°$ and a polar angle of $84°$ from the beam line, as can be seen in Figure 2.4b [22]. The positioning of milliQan in the PX56 drainage gallery would also add a shielding of 17 m of rock to the experimental cavern and would still lie about 73 m underground.
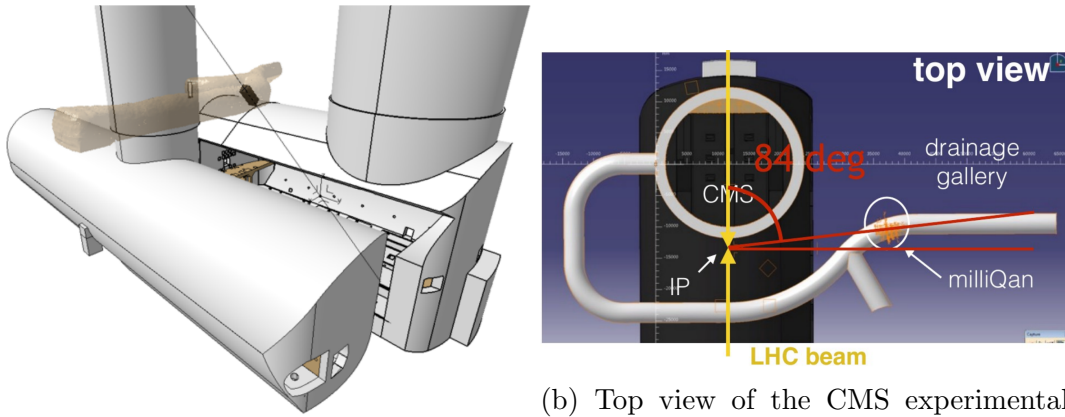
(a) 3D view of the CMS experimental cavern and the PX56 drainage gallery [22].

(b) Top view of the CMS experimental cavern and the PX56 drainage gallery.

Figure 2.4: A top view and 3D model of the CMS experimental cavern and the PX56 drainage gallery, showing the chosen location for milliQan.

2.2.3   The milliQan Demonstrator

Awaiting the funding for the full detector, the milliQan collaboration installed a 1% demonstrator at the PX56 drainage gallery in 2017. This demonstrator, shown in Figure 2.5, consists of eighteen scintillator bars spread out over three layers of 2×3 scintillator+PMT units [25]. In addition, "slabs" and thin panels of scintillator have been added to tag charged particles like muons from the IP, study radiation backgrounds and to simulate the active veto of the full detector. Also hodoscope packs were planted on distinct points along the detector composed of small arrays of plastic scintillator which are readout via SiPMs. These can provide more precise information about the position of a charged particle and allow for a crude tracking through the demonstrator [25].

After its installation, the demonstrator has been used to perform mCP searches throughout 2018. These searches rely on a triple coincidence of pulses across three layers of the milliQan demonstrator [25]. An interesting measure that was observed was the dependence of the total number of particles identified as having a muon pulse in all four slabs on the integrated luminosity of the LHC. As can be seen in Figure 2.6, there is a clear linear dependence, which provides confidence that the demonstrator was correctly aligned and performs as expected.

The main goal when performing searches for mCPs (or, generally, any type of new physics) is background rejection. There are four main sources of background which need to be accounted for when performing mCP searches with this demonstrator

Dark rate overlap Each PMT has a dark current. This can arise as a result of effects like thermal emission of electrons from the cathode. The simplest background source comes from random overlap of three such dark

(a) Schematic view of the milliQan demonstrator.

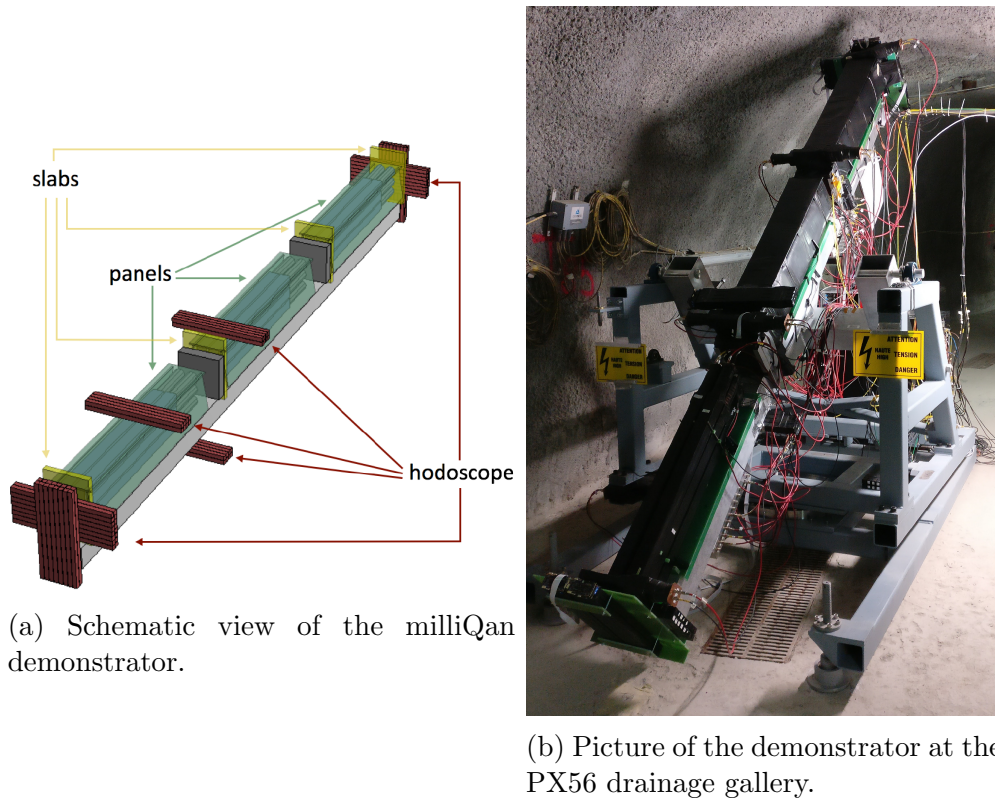(b) Picture of the demonstrator at the PX56 drainage gallery.
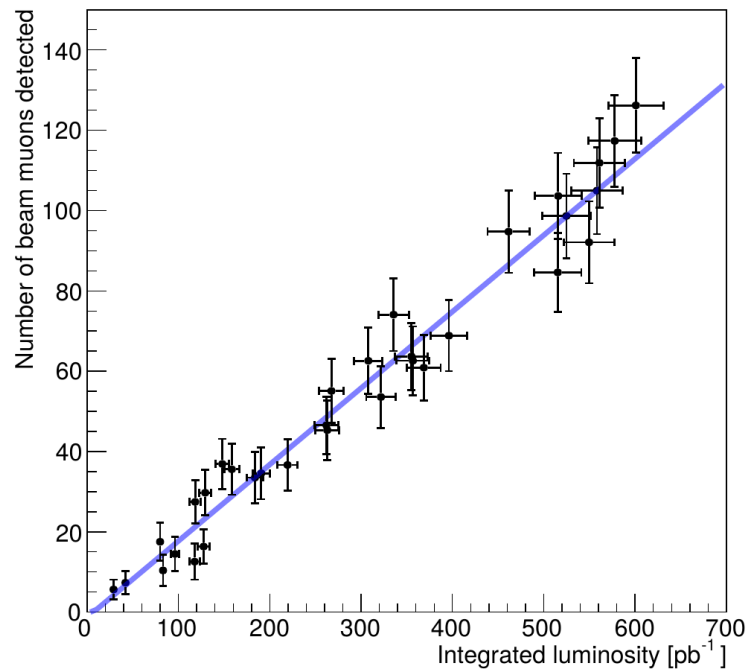
Figure 2.5: The milliQan demonstrator.

Figure 2.6: The total number of particles identified as having a muon pulse in all four slabs as a function of the LHC luminosity [25].

rate pulses [25].

Radiation This concerns any type of radiation in the cavern, in the scintillator bars or in the surrounding material. Some of this radiation can induce correlated deposits in several bars.

Muon showers As mentioned earlier, muons arising from the LHC (through Z, W or $t\bar{t}$ production) are an important background source. However, muons can also emerge from cosmic rays. While through-going muons can be efficiently vetoed, a large number of gammas, neutrons and electrons may be caused by an interaction of a cosmic ray muon with the rock in the drainage gallery. This could result in a pulse in each layer of the milliQan demonstrator.

Afterpulses Afterpulses arising from correlated deposits may overlap and produce triple coincidence hits [25].

When applying event selections in order to reject contributions of these background sources, it is important to understand their behaviour. When considering the radiation, for example, as a background source, lead bricks have been placed in between the different layers (see Figure 2.5a) as to decrease the probability of correlated hits from resulting photons or electrons in different layers. However, as there is no shielding between adjacent bars in the same layer there is no information about possible coincidence hits among those bars.

Another source of background whose behaviour could be very relevant are the cosmic muon showers. As cosmic rays are, generally speaking, ubiquitous, it can be interesting to get an idea of how this external background is distributed.

This thesis will attempt to tackle these two specific sources of background. On the one hand the presence and properties of internal radiation of the scintillator bars will be studied in detail in Chapter 3. On the other hand, the angular distribution of the external cosmic muon showers will be more closely examined in Chapter 4. Knowing how important these backgrounds are and how they behave, is relevant information to increase the performance of the demonstrator and, by extension, the future milliQan detector itself.

Chapter 3

Internal Background

3.1 Introduction

The most important internal background that has not already been accounted for by other means is the possibility of correlated hits in adjacent bars. When considering two bars, placed side by side, a distance Δx away from each other one can measure any event which leaves a hit in both bars within a certain time frame. There are now two possibilities: either a certain form of external background (mostly cosmic radiation) caused two independent hits (one in each of the bars) within that time frame, or only one of the two bars detected a hit produced by external background which caused the production of a secondary electron with enough energy to escape a significant distance away from the primary radiation beam and produce further ionization in the adjacent bar. Collectively such secondary radiation is defined as *delta radiation.*

Within a bar events coming from cosmic muons traversing the scintillator can be easily distinguished by looking at the distribution of the height of the first pulse as shown in Figure 3.1. This quantity was measured in analogue-to-digital-converter (ADC) counts. This distribution shows a clear upsurge starting at 600 ADC counts. Any event with such a high pulse height can almost certainly be attributed to a cosmic muon. The peak close to zero must come from some other background. By studying the distribution of the time difference between the hits in the two bars and how this distribution evolves in function of the distance between the bars, information about the nature of this internal background can be obtained. As the LHC has been going through a long shutdown, we were able to perform the necessary background measurements in November 2019 at the PX56 Drainage Gallery.
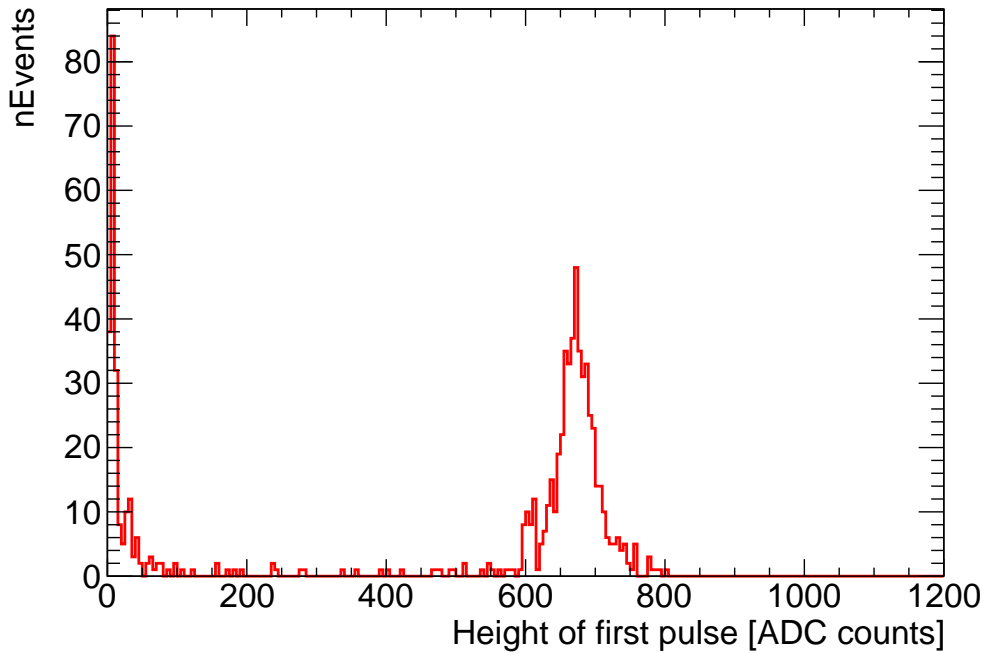
Figure 3.1: Distribution of the height of the first pulse in channel 1 given in ADC counts.

3.2   Methodology

The setup used for this experiment is shown in Figure 3.2a. When studying this image closely it can be noticed that the left scintillator is connected to two PMTs (linked to channels number 15 and 28) as opposed to the right bar, which is only connected to one PMT (linked to channel number 21). The distance between the bars was measured with a tape measure (up to 1 mm accuracy) and after turning off the lights (ensuring complete darkness) a run was started and these bars were left to take data. Such a run consists of detecting events which produce hits in both bars within a certain time frame, measures the time and amplitude of each pulse and stores this information in a ROOT-tree. After a chosen amount of time the run was stopped, the cavern was illuminated, the bars were placed further apart and the same process was repeated. This was done for three different distances: 10 cm, 30 cm and 50 cm. In order to find information about possible correlated hits due to secondary radiation, these measurements were redone at the same three distances, this time with shielding placed centered in between the two bars (see Figure 3.2b). This shielding existed of four legs of a (then) yet to be installed metal cabinet. Even though the exact material and density of these legs is unknown, they conveyed the impression of being massive and were assumed to provide decent protection from possible secondary radiation.

An overview of the duration of each run can be found in Table 3.1. The variety
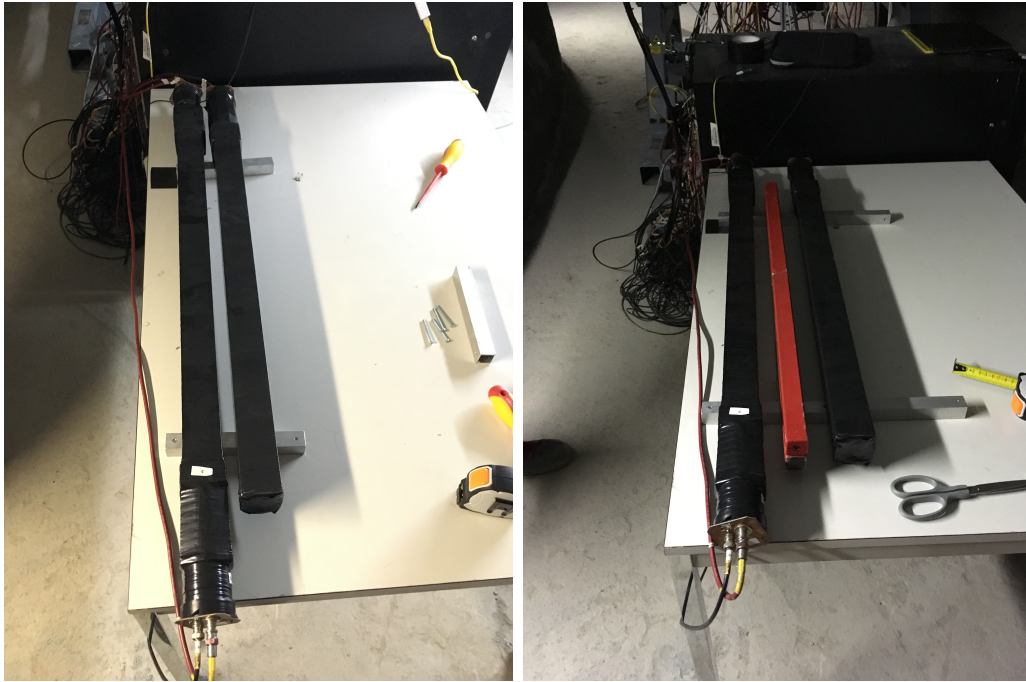
(a) Bars placed side by side without shielding.

(b) Bars placed side by side with shielding.

Figure 3.2: Scintillator+PMT units placed side by side on a table in the PX56 drainage gallery.

of these durations can be attributed to inconveniences linked to the schedule of the day these experiments were performed rather than having a scientific background.

Table 3.1: Duration of each run with and without shielding.

Δx	Runtime without shielding	Runtime with shielding
10 cm	576 s	828 s
30 cm	612 s	612 s
50 cm	11 016 s	720 s

An extra experiment was conducted when the bars were placed 30 cm apart. In the shielding a small "window" of 10 cm wide was created as shown in Figure 3.3. This was done with the aim to identify whether possible secondary radiation emerges from the plastic scintillator or from the attached PMTs.

An initial idea proposed to do the same analysis above ground in a dark room. This experiment was planned to be conducted during the Spring of 2020 at the Vrije Universiteit Brussel (VUB). The same scintillators and PMTs were transferred to Brussels but due to the COVID-19 pandemic outbreak, all universities had to close and this analysis could not be performed.
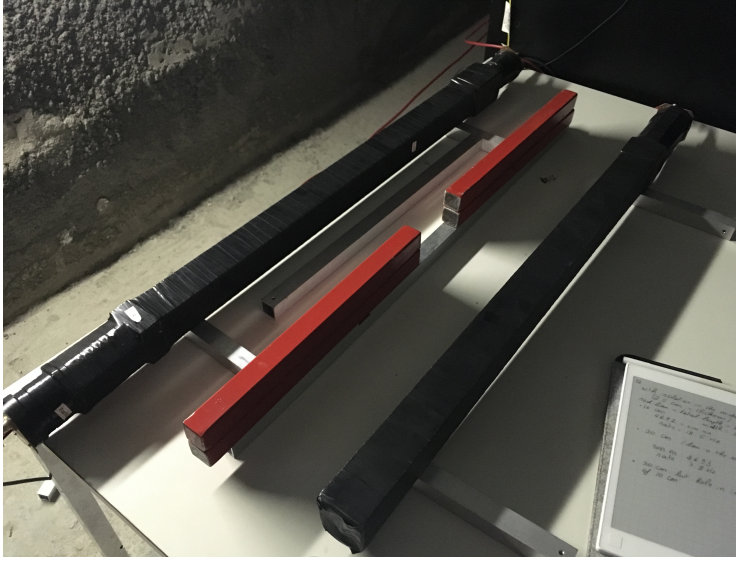
Figure 3.3: Setup where the bars were placed $30\,\mathrm{cm}$ apart and a $10\,\mathrm{cm}$ gap was created in the shielding.

3.3 Results

In order to find information about the nature of the internal background, it is sensible to first categorize the events in two groups: those that, apart from creating a hit in both bars on the table, also produced a hit in any other bar connected to the milliQan demonstrator whose height of the first pulse is larger than 600, which will be referred to as *cosmics*, and those that satisfy the complement of this condition, which will be referred to as *non-cosmics*. For a cosmic event the different hits are thus most probably caused independently by different particles originating from the same shower, while the non-cosmics are most probably the result of any internal background between the two scintillators.

For the different distances (with and without shielding) the time difference of the hits between the two bars was considered both for the cosmics and non-cosmics separately. Here the time difference Δt is defined as the time linked to the largest pulse in the bar on the left in Figure 3.2 minus the time linked to the largest pulse in the bar on the right in Figure 3.2. The fact that the left scintillator was connected to two PMTs was used to our advantage when defining Δt

$$\Delta t \equiv \begin{cases} t_{28} - t_{21} & \text{if } N_{28} \neq 0 \\ t_{15} - t_{21} & \text{if } N_{28} = 0 \text{ and } N_{15} \neq 0 \,, \end{cases} \tag{3.1}$$

where N_k represents the number of pulses measured in channel number k. By defining Δt this way, it suffices that only one of the two PMTs in the left scintillator detected a certain event. For each event, Δt was calculated and its values were placed in a histogram. The peak of the histogram was then

fitted using a Gaussian distribution to gain information about the position and spread of the distribution. An example of such a histogram can be seen in Figure 3.4a which represents the Δt-distribution for non-cosmic events detected at a Δx of 50 cm. The events are distributed around an average of -5.10 ± 0.04 ns with a spread of 9.52 ± 0.03 ns. These seemingly odd values for Δt can be attributed to the time calibration of the PMTs. The position of the peak of the distribution therefore does not have a physical meaning. This is not a problem as it is also not really of interest where the peak lies, but rather how the distance between the two bars and the presence of shielding influences the position of the peak and the shape of the distribution.
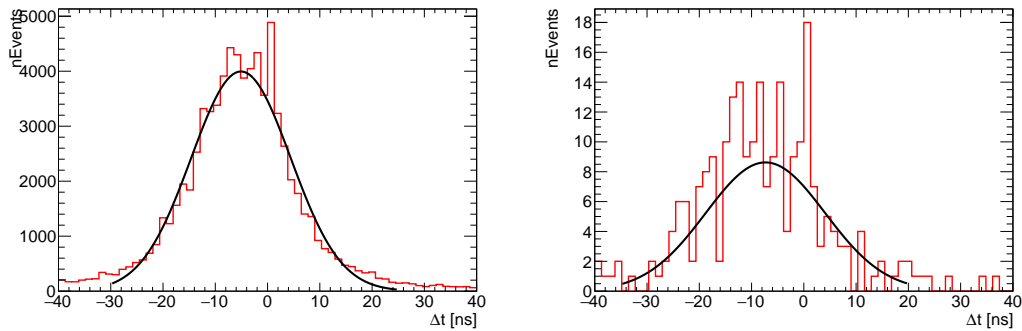
(a) Δt-distribution of non-cosmics for bars placed 50 cm apart.

(b) Δt-distribution of cosmics for bars placed 50 cm apart.

Figure 3.4: Distributions of the time difference of the largest pulses between the two bars. The bars were placed 50 cm apart and no shielding was placed between them.

In Figure 3.4b the same histogram was created for the cosmic events. The fitted peak in this plot is formed around an average of -7 ± 1 ns with a spread of 11 ± 1 ns. As such events are much more scarce a well defined peak is absent which makes it also very hard to fit with a Gaussian. It is also not a coincidence that Figure 3.4 represents the Δt-distributions for the experiment where the bars were placed 50 cm apart without shielding between them. When looking back to Table 3.1, it can be seen that the duration for this experiment was significantly longer than any of the other experiments which only detected a mere handful of cosmics in the brief time they took data.

When only considering the results of the fit, it would seem that there is no dissimilarity in the mean time difference between cosmic and non-cosmic events. A closer look at both distributions in Figure 3.4, however, learns that there is a rather odd peak at $\Delta t = 0$, which has also been observed in the Δt-distributions for all the other distances. The cause of this peak is unknown, yet the problem will most likely lie in the algorithm responsible for determining the time stamp. Even though this peak does not seem to influence the Gaussian fit in Figure 3.4a, the fit of the cosmic distribution in Figure 3.4b (which is much more sensitive to such disruptions due to the little amount of

data) seems as if it is slightly shifted to the right. If this is indeed the case, this would mean that the average time difference is lower for cosmics than non-cosmics, which would be consistent with the idea that cosmics are uncorrelated coincidental hits while non-cosmics are the result of internal background and will, on average, show a delay in the Δt-distribution. This delay would then be attributed to the time the secondary radiation needs to travel between the two bars. Nevertheless, since the number of cosmics detected is so low, this remains speculation and ideally this study should be done again with much longer runs.

The original idea consisted of comparing how the Δt-distributions for cosmics and non-cosmics are influenced by the distance between the two bars. However, since the data did not contain enough cosmics to accurately fit the Δt-distributions with a Gaussian, it was opted to study the impact of the distance on the Δt-distribution of the entire data set.

Figure 3.5 shows the fitted parameters concerning the position and the spread of the peak of the Δt-distribution for each conducted experiment. Here the red curves represent the measurements without shielding, the green curves represent those with shielding and the single blue dots represent the measurements for the experiment with the 10 cm window in the shielding. When considering the graph in Figure 3.5a, a first thing that stands out is the fact that most uncertainty bars are very large with respect to the variations in the average time difference Δt. This is a direct consequence of the short duration of certain runs. As a result, only the measurement at a 50 cm distance without shielding has an acceptable uncertainty. For the other measurements it can be noticed that both distance as well as the presence of shielding have an impact on the uncertainty. This is a first indication that these elements also influence the event rate.

This idea is reinforced when contemplating the graph in Figure 3.5b. It becomes clear that the spread of the Δt-distribution increases with distance. This behavior can only be explained when a significant amount of the detected events are due to secondary radiation within the bars as the main reason for this increase in spread is because the pathlengths of secondary radiation increase in both travel directions. Furthermore, there seems a priori no physical reason why any external background would show this dependence on distance.

In order to confirm these indications, the event rate was analyzed for each of the above mentioned experiments. The results of this analysis can be found in Figure 3.6 where the same color code was used as in the plots in Figure 3.5.

As the event rate goes down in function of the distance, it can be concluded that most of the events are in fact correlated. This conclusion is further confirmed by the fact that placing shielding in between the bars makes the rate drop significantly. Yet, even with shielding, some delta rays can still pass through
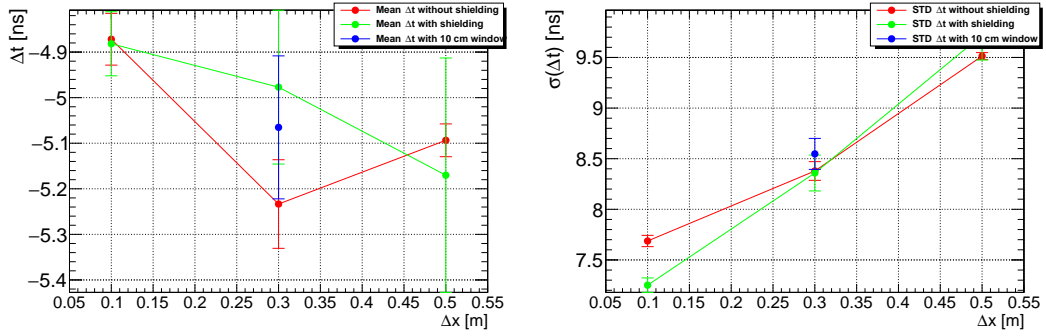
(a) Fitted position of the distribution in function of Δx

(b) Fitted spread of the distribution in function of Δx

Figure 3.5: The fitted values for the position μ and spread σ of the Δt-distribution in function of a distance.

as also here the event rate decreases with increasing distance. The fact that the blue cross lies above the green curve also appears to show that the correlated hits actually originate in the scintillator rather than be attributed to some interactions in the PMTs.

The impact of the shielding can be further quantified by considering the ratio of the event rate with shielding R_S over the event rate without shielding R_{NS}, which will be called ξ

$$\xi = \frac{R_S}{R_{NS}} \, . \tag{3.2}$$

This fraction has been plotted in function of the distance and is shown in Figure 3.7. This plot shows that ξ depends weakly linearly on Δx, meaning that there is only a small fraction of the measured events which are not correlated.

It is thus clear that the bars in the demonstrator detect a vast amount of internal background caused by delta radiation. When installing the milliQan detector it is important to take into account that some form of shielding around the bars which would stop some of the secondary radiation is desirable. This secondary radiation should also be taken into account when analyzing data taken with the scintillator bars and a proper simulation of this effect is thus required.
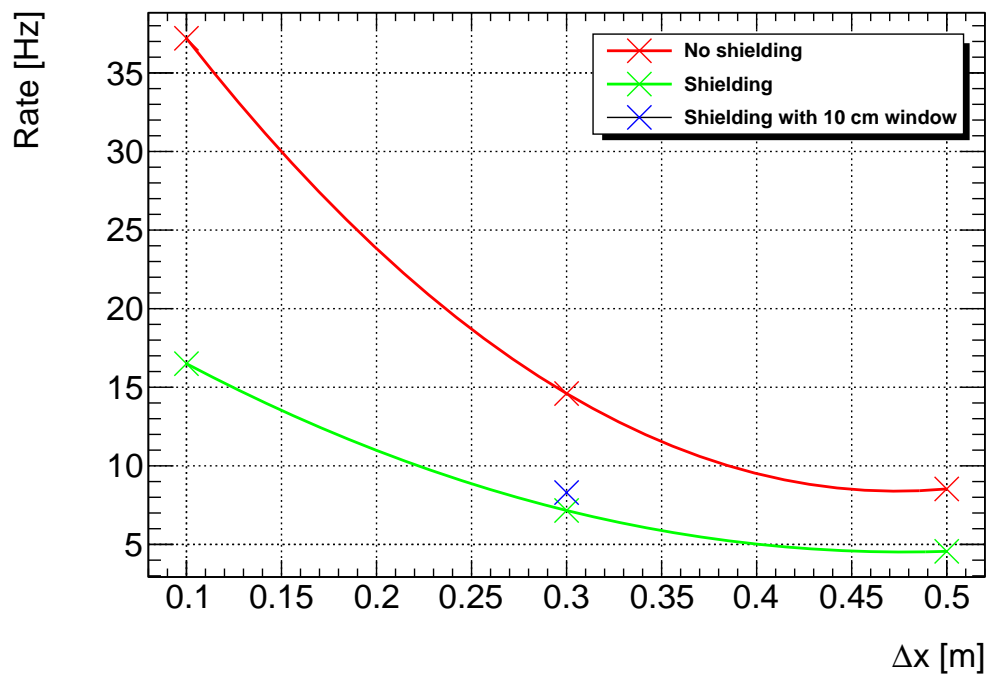
Figure 3.6: Event rate in function of the distance between the bars, Δx, given with shielding, without shielding and (at one distance) with a 10 cm window in the shielding.
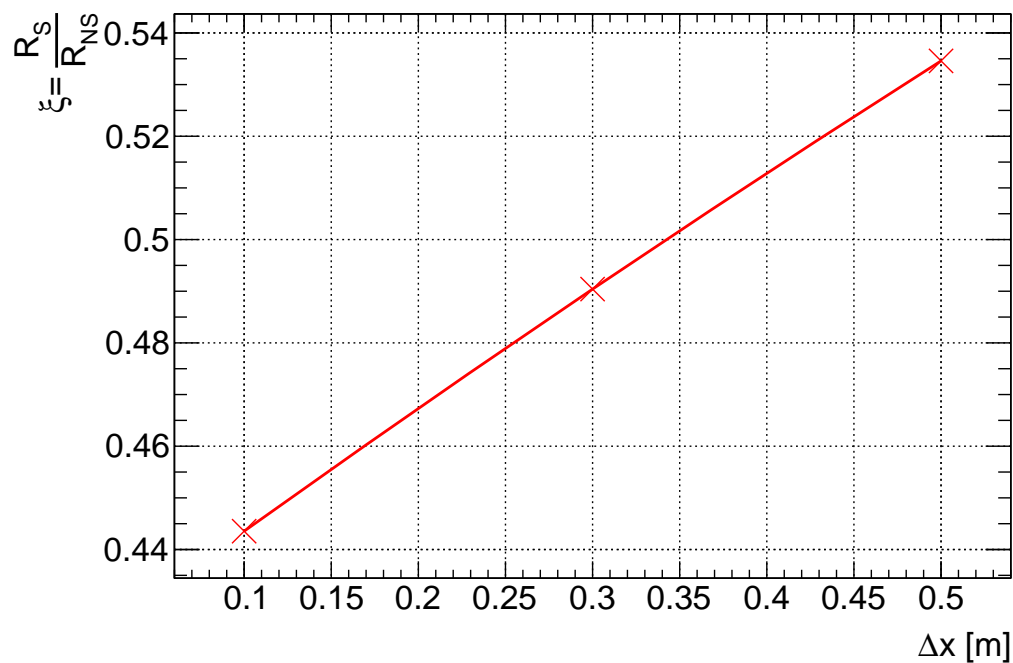

Figure 3.7: Ratio of the event rate with shielding over the event rate without shielding in function of the distance Δx between the two bars.

Chapter 4

External Background

4.1 Introduction

Even though the milliQan demonstrator is positioned 70 m underground, still a relevant amount of cosmic radiation is expected to influence the measurements either directly or, as discussed in the previous chapter, due to secondary radiation in the bars. Knowing how this external background is distributed is important to be able to anticipate what kind of events can be expected, which is especially interesting when constructing a simulation for the full milliQan detector. When the milliQan demonstrator was taking data in 2018, it was assumed that the cosmic radiation follows a $\cos^2(\theta_{\mathrm{zenith}})$ distribution [26]. Even though this is true on the surface of the earth [27], it is not certain whether this assumption is also valid 70 m underground.

The angular distributions of this external background can be measured by adding some sort of tracking material in the PX56 drainage gallery and letting it take data for a long period of time. The task then consists of fitting the three-dimensional tracks and abstracting the angles from this fit.

4.2 Methodology

4.2.1 Experimental Setup

In chapter 2 it was mentioned that hodoscopes are attached to the milliQan demonstrator. These hodoscopes exist of two packs of eight long thin arrays of plastic scintillator and were originally used to provide more precise information about the position of a charged particle, and can thus serve as decent tracking material. In November 2019, we removed the four hodoscopes from the demonstrator and placed them perpendicular on each other under the demonstrator in a Jenga-like pile as shown in Figure 4.1. This way information about the height, width and depth of the trajectory of a particle can be attained. The

data that was used for these studies were taken between November 7 until
November 27 at 3:12 pm.

Figure 4.1: The hodoscopes were placed in a Jenga-like pile under the demonstrator such that tracking could be performed in both directions.

4.2.2   Data Acquisition

Each of the long thin scintillator arrays, or *fingers* as they will be referred to, is
readout by a silicon photomultiplier and is linked to a certain channel number.
The efficiency of these fingers is virtually 100 %. When an ionizing particle
triggers the hodoscope pile, the event is readout according to the following
format:

```
1573084803 2019:11:07:00:00:03:150606 0 1 0 0 0 1 0 0 0 0 0 0 0 0
0 0 0 0 0 0 0 1 1 0 1 0 0 0 0 0 0 0 0 0 0 0 0 0 0 0 0 0 0 0 0 0 0
0 0 0 0 0 0 0 0 0 0 0 0 0 0 0 0 0 0 0 0 0 0 0 0 0 0 0 0 0 0 0 0 0
0 0 0 0 0 0 0 0 0 1010 2.704039 214317401
```

Here the blue and green digits represent the UNIX epoch time and the real
time respectively, both according to the coordinated universal time (UTC).
After these time stamps the readout of the different channels start. The first
64 bits (shown in purple) are the readout of each of the fingers of the hodoscope
pile: a one means that the finger was hit, a zero means it was not hit. The
subsequent string of orange bits correspond to the channels of the track packs
which are placed on the demonstrator. The red bit which follows, serves as a
flag informing whether the readout was triggered by the hodoscopes and track
packs themselves (i.e. *internally triggered*, when the bit is zero) or by an event
in one of the bars or slabs still connected to the demonstrator (i.e. *externally
triggered*, when the bit is one). As most of the externally triggered events are
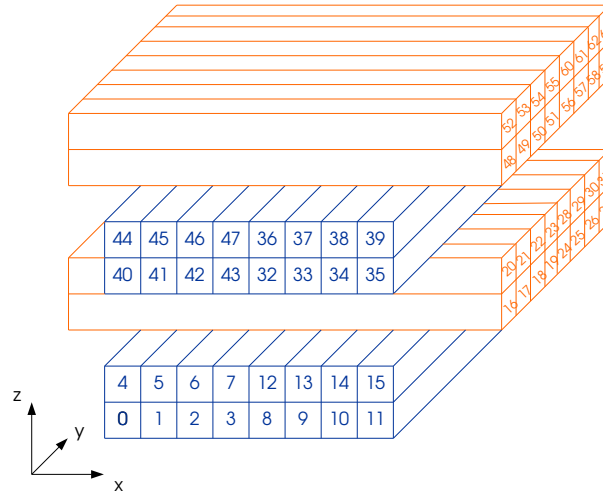
Figure 4.2: Sketch of the hodoscope pile depicting on each finger the corresponding channel number.

empty in the hodoscopes, this analysis will focus only on the internally triggered events. The last couple of digits provide some more information about externally triggered events and are, as such, not relevant for this analysis.

Figure 4.2 shows a sketch of the hodoscope pile where each of the fingers have been labeled with their respective channel number. This number corresponds to the position of the bit in the data string: the first bit in the purple string corresponds to the readout of channel number zero in Figure 4.2, the second bit corresponds to channel number one, etc.

The objective now consists of attributing a three dimensional position to each hit in an event. A right-handed Cartesian coordinate system was set up in such a way that the z-axis points upwards, the y-axis lies parallel with the demonstrator and points in the direction of the interaction point and the x-axis is determined by the right hand rule. In this thesis, the hodoscope pile was then divided into eight *layers* numbered from 0 to 7, counting from bottom to top. Each of these layers then consist of eight fingers, also each given an index from 0 to 7. The horizontal position of a hit can be attributed to the center of the finger, following a uniform distribution between the edges. As these fingers have dimensions $2\,\mathrm{cm} \times 2\,\mathrm{cm} \times 45\,\mathrm{cm}$, the origin of horizontal axis was aligned with the edge of the finger with index 0, such that the center of the first finger corresponds to a horizontal position of $1\,\mathrm{cm}$. As a consequence, if a finger with index j was hit, this index was mapped to a horizontal coordinate of $2j + 1$. Figure 4.3 clarifies this explanation by picturing the horizontal axis used next to a sketch of an array. The same startegy was applied for the vertical position, this time using the layer number as index. Whenever two fingers next to each

other were both hit, the edge separating the two fingers (rather than the center
of one of the two fingers) was used to position the hit.

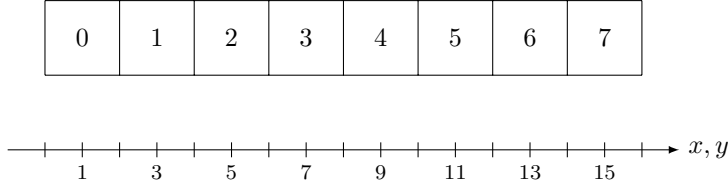| 0 | 1 | 2 | 3 | 4 | 5 | 6 | 7 |

Figure 4.3: Drawing of a layer above a horizontal position axis with the used
scale.

The uncertainty on the position was determined by calculating the square
root of the variance of a stochastic variable X which is uniformly distributed
between the two edges of one finger. Let a and b define these two edges ($a < b$)
and $\ell \equiv b - a$ define the width of a finger. The probability density function is
then given by

$$f_X(x) = \begin{cases} \frac{1}{\ell} & \text{if } a < x < b \\ 0 & \text{elsewhere}, \end{cases} \tag{4.1}$$

with expectation value the mean value of a and b: $E[X] = \frac{a+b}{2}$. The expecta-
tion value of X^2 can now be calculated as follows

$$\begin{aligned} E[X^2] &= \int_a^b x^2 f_X(x)\,\mathrm{d}x \\ &= \frac{1}{b-a} \int_a^b x^2 \,\mathrm{d}x \\ &= \frac{b^2 + ab + a^2}{3}. \end{aligned}$$

This delivers all the information needed to achieve an expression for the vari-
ance $\mathrm{Var}[X] = \sigma^2$

$$\sigma^2 = E[X^2] - E[X]^2 = \frac{\ell^2}{12}. \tag{4.2}$$

Before continuing, it needs to be mentioned that this analysis assumes a certain
simplification. As can be deduced from the sketches in Figure 4.2 and 4.3, it is
assumed that adjacent fingers and layers are joined by their edge, suggesting
that there is no space in between them. A closer look at the setup in Figure 4.1
shows immediately that this assumption is not a representation of the reality.
In principle this is not a problem when all the fingers are in equal distance
separated from each other: the distance between two centers of adjacent fingers
is defined as 2 units, half that distance is then one unit in the used scale.
However, it can also be seen in Figure 4.1 that, as each hodoscope is composed
of two packs linked to each other, the two fingers in the middle of the layer
are placed further away from each other. Since it was unknown how much

more these fingers were separated from each other, this extra spacing was initially ignored. In section 4.3 it will become clear that this will not impact the results.

Now that a process has been established on how to get the positions of the hits in each event, the trajectory of the particle still needs to be fitted. Since the magnetic field in the drainage gallery was measured to be $2\,\mathrm{mT}$ when the CMS detector is active [26], there is no reason to assume that the particle will follow anything else than a straight trajectory and the points were linearly fitted in both x- and y-directions

$$f_x(x) = a_x x + b_x \tag{4.3a}$$
$$f_y(y) = a_y y + b_y\,, \tag{4.3b}$$

From the fitted values for the slope, the angles under which the particles hit the hodoscope pile can be obtained

$$\theta = \arctan(a_x) \tag{4.4a}$$
$$\phi = \arctan(a_y)\,, \tag{4.4b}$$

where θ (resp. ϕ) is the angle measured with respect to the x-axis (resp. y-axis). Another interesting observable that can be obtained is the point where the fitted trajectory intersects the $z = 0$-plane, i.e. where it hits the "virtual" ground. This is simply obtained by inverting equations (4.3a) and (4.3b)

$$x_0 = -\frac{b_x}{a_x} \tag{4.5a}$$

$$y_0 = -\frac{b_y}{a_y}\,. \tag{4.5b}$$

An example of a successful fit of a particle trajectory can be found in Figure 4.4. In these plots the positions in the (x, z)- and (y, z)-planes are plotted with their respective error bars according to the calculation described above.
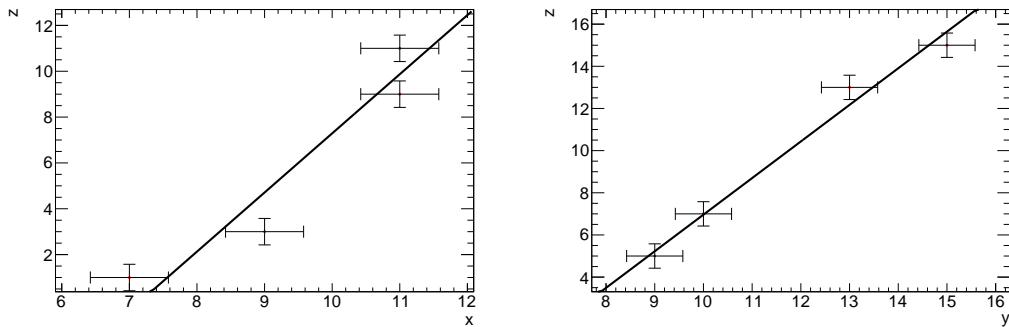
(a) Fit in the x-direction   (b) Fit in the y-direction

Figure 4.4: Example of a fit in both x- and y-direction

By performing the inverse calculation, the original channels which were hit can be found and are reconstructed in Figure 4.5.
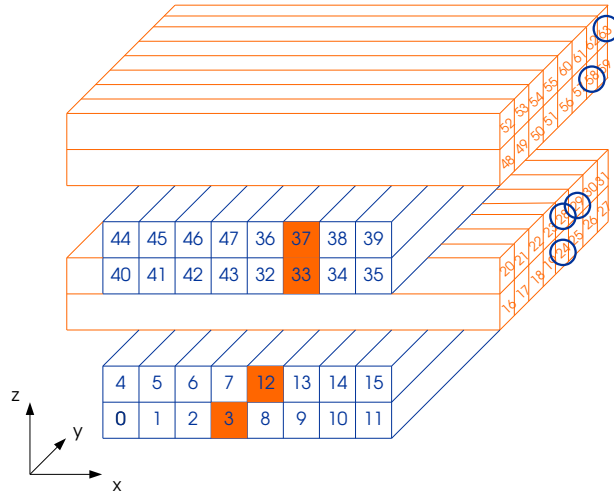
Figure 4.5: Reconstruction of the event corresponding to the fit shown in Figure 4.4

4.2.3   Basic Event Selections

When performing the analysis, it became clear that not every event could be fitted as easily as the example in Figure 4.4. A first basic requirement is that for a fit to perform well, not only enough points are needed, but the points need to be distributed over two different hodoscopes. If a good fit in both directions is desired, at least seven layers need to be hit for this condition to be certainly satisfied. If, for example, the two bottom layers are not hit (and thus only a total of six layers is used), the points in the y-direction can be fitted nicely, yet the two hits in the x-direction will allow too much freedom for a reliable fit. However, when looking at Figure 4.1, it can be seen that the part where all the hodoscopes overlap is rather small compared to the pieces that protrude in either the x- or y-direction. It is therefore sensible to require that an event is "fittable" in at least one of the two horizontal directions or, in other words, that at least three points can be used in each direction.

A second requirement arises when considering events where in one layer more than two adjacent 1's were readout or where multiple hits occurred in the same layer which were not adjacent. An example of such an event is shown here below, where the left (resp. right) column shows the readout of the hodoscopes placed in the x-direction (resp. y-direction):

```
-------- 11110000
-------- 11110000
00000100 --------
00000100 --------
-------- 00001100
-------- 00000100
10001000 --------
00010000 --------
```

The bottom hodoscope in the x-direction displays two ones which are not adjacent while in the left upper corner of the y-direction the entire pack lit up. It is obvious that such events will not deliver good fits. Therefore such events, i.e. events witch contain a layer where nonadjacent hits are present or where there are more than two adjacent hits present, were not used for this analysis.

Before analyzing the results, a last remark concerning the "fittability" should be made here. Due to the requirement that at least three different layers need to be hit in either of the two directions, the smallest angle that can be theoretically achieved by a fit is 29.7°. This implies that a vast amount of the analyzed events will have a very steep slope. As a result, particles which hit the hodoscope pile under an angle of 90° with the horizontal plane (or any angle within a 15° interval of 90°), will be fitted with a slope of practically infinity, and resulting numerical instabilities will distort the angular distribution significantly. In order to bypass this problem, the horizontal and vertical coordinates of the position points were switched before performing the fit. This way, a particle which falls in very steeply can be safely fitted with a small slope and, since the minimum amount of layers that need to be hit does not allow events which fall in under an angle lower than 29.7°, there is no danger in fitting the curve with the switched coordinates. The required information can then easily be obtained from the fitted parameters as has been made clear in Figure 4.6.
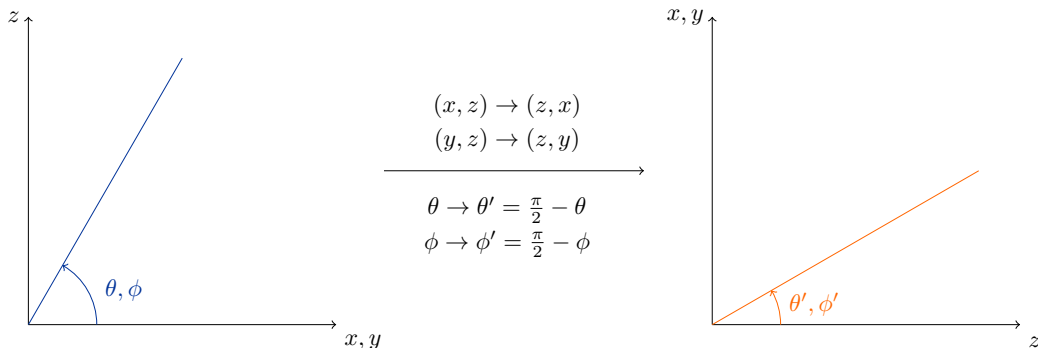

Figure 4.6: Sketch showing how the relevant observables transform under the switching of the horizontal and vertical coordinates.

4.3   Results

4.3.1   Analysis Using the Full Hodoscope Pile

Letting the hodoscope pile run during a large part of November delivered a data set containing a little over 3.5 million events of which 559 132 were internally triggered. Of these events 66 414 passed the event selection discussed in the previous section in the x-direction and 69 208 passed the selection in the y-direction. Applying the method elaborated in the previous section, the θ- and ϕ-distributions were plotted and are shown in Figure 4.7.

(a) θ distribution (x-direction)   (b) ϕ distribution (y-direction)
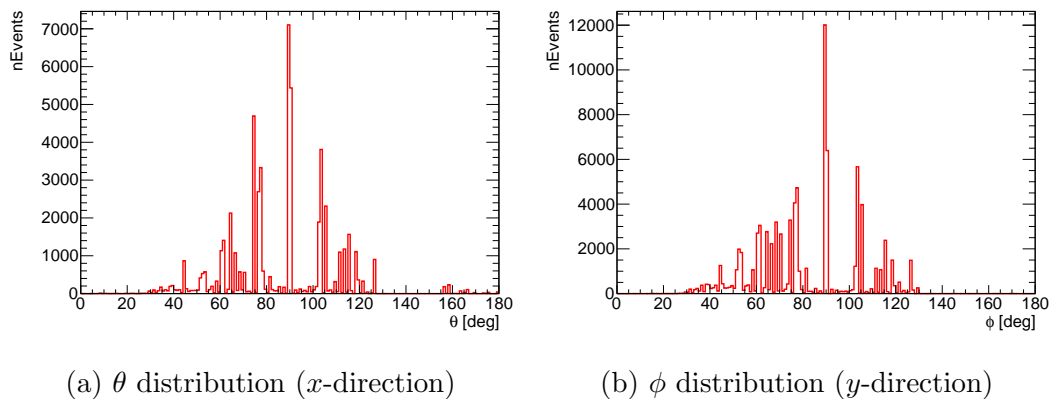
Figure 4.7: Angular distributions in both directions.

A first thing that stands out in these histograms is the fact that the distributions show peaks at certain values, while showing smaller fluctuations around each peak. This is a direct consequence of the relatively poor granularity of the hodoscopes. Since the fingers are rather large compared to the total tracker pile, the positioning of the hits is coarsely discretized and, as a result, the angular distributions will also show a discrete pattern. Events where two adjacent hits occurred in the same layer are a source of the variations in between the peaks.

A second thing that can be noticed in these distributions is that a certain asymmetry arises. Once over 130° the number of events drop to zero (apart from a handful of events around 160° which were all found to be badly fitted), while on the left side the distribution keeps decreasing until 30°. This asymmetry becomes even more visible when looking at the distributions of the intersection points with the $z = 0$-plane (or, in other words, the *roots* of the linear fit) which are shown in Figure 4.8. Recall that positions 0 and 16 define the edges of the hodoscope pile.

In the x-direction, the distribution stops abruptly once over 18 (apart from the little upsurge at 25, which correspond to the badly fitted events around 160° in Figure 4.7), while falling off a little more slowly on the left side of the detector. This asymmetry becomes more clear in the y-direction. As the
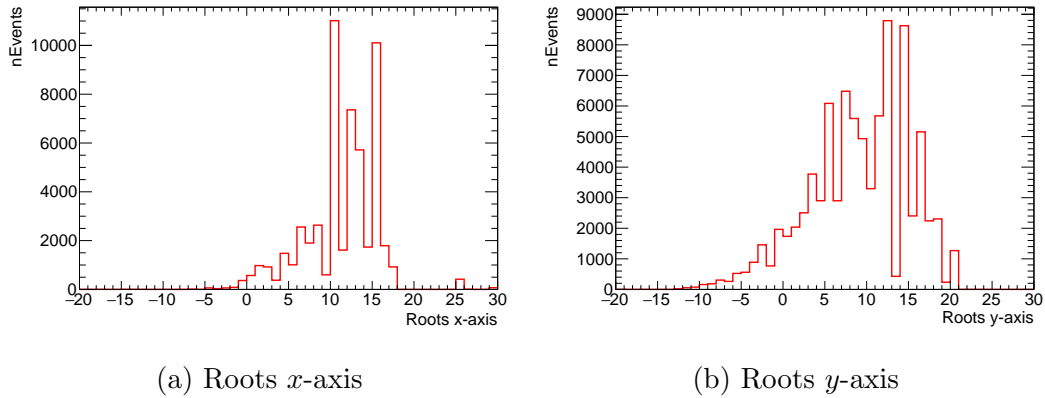
(a) Roots x-axis   (b) Roots y-axis

Figure 4.8: Distribution of the points of intersection with the $z = 0$-plane in both x- and y-directions.

lowest hodoscopes in this direction lie on top of the bottom hodoscopes (which point in the x-direction), the distribution of y-roots will reach further outside the edges of the hodoscope pile. On the right side of the hodoscope pile the distribution stops abruptly at 20 while on the left side it falls off slowly until it reaches -12.

Another, seemingly paradoxical, asymmetry occurs within the edges of the hodoscope pile. Though this is much more prominent in the x-direction, a significant lower amount of events is located at roots under a value of 10 in both directions. This appears to contradict the previous asymmetry (which is only visible outside the edges of the hodoscope pile) which shows that there is an excess of events which were fitted with low angles and, intuitively speaking, should induce more events with lower roots, also within the edges of the hodoscope pile.

In order to better understand this effect, the distributions of the roots and angles have been placed in two-dimensional histograms, as can be seen in Figure 4.9.

As expected, the distributions of the roots show a linear dependence on the angular distributions. Also here both asymmetries can be found: there are more events with an angle lower than 90° which results in more events with a root on the left side of the hodoscope pile than on the right side, but within the edges of the pile more events can be found with a root under a value of 10 than above this value.

In these plots, however, some more information about the nature of these asymmetries can be gained. When focusing on those events which have a very steep angle (i.e. angles between 85° and 95°), it can be seen that below a certain root-value (which in both directions still lies within the edges of the hodoscope pile), such steep events are nonexistent. This is a rather odd observation as one would expect that these types of events would be uniformly
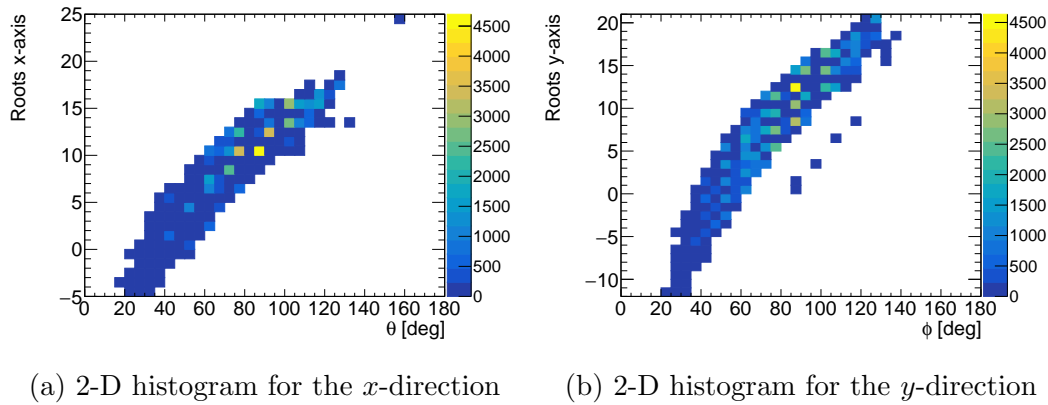
(a) 2-D histogram for the x-direction   (b) 2-D histogram for the y-direction

Figure 4.9: Two-dimensional histograms displaying the distributions of the intersection points with the $z = 0$-plane in function of the angular distributions.

distributed between the edges of the hodoscope pile.

4.3.2   Testing the Functionality of the Hodoscopes

These results convey the impression that something might be wrong with some of the hodoscopes. In order to verify this, a test was performed, consisting of observing the distribution of events where two hits right above each other (and thus in the same hodoscope) occurred, while the rest of these two layers was not hit. If all the hodoscopes were to work as expected, these type of hits would be uniformly distributed as this selects clean cosmics layer by layer.

The two-dimensional histograms showing the distribution of these *pairs* of hits for both x- and y-direction can be seen in Figure 4.10. Here it was opted to use the finger indices as horizontal coordinate and hodoscope indices (the two bottom layers serve as one hodoscope with index zero, the next two layers form a hodoscope with index one etc.) as vertical coordinate as the objective here is to identify what parts of the hodoscope pile are possibly defective.

We will first consider the two-dimensional histogram for the x-direction in Figure 4.10a. What is most noticeable here are the empty spots in the left upper pack and the gap at index 4 of the bottom hodoscope. Such a gap is either an indication that one or multiple fingers simply do not work or that something is wrong with the readout in the sense that if one finger is hit certain adjacent fingers are also hit.

To further investigate this, it is sensible to look at how often each individual channel reads out a hit. In Figure 4.11 these values have been placed in a histogram, showing also the same picture from Figure 4.2 as to easier link a channel to its corresponding finger in the hodoscope pile. In this histogram it can be seen that channel 8, which corresponds to a finger in the bottom layer with index 4, is never hit and is therefore most likely defective. This explains the gap in the bottom hodoscope in Figure 4.10a. There are also some strong
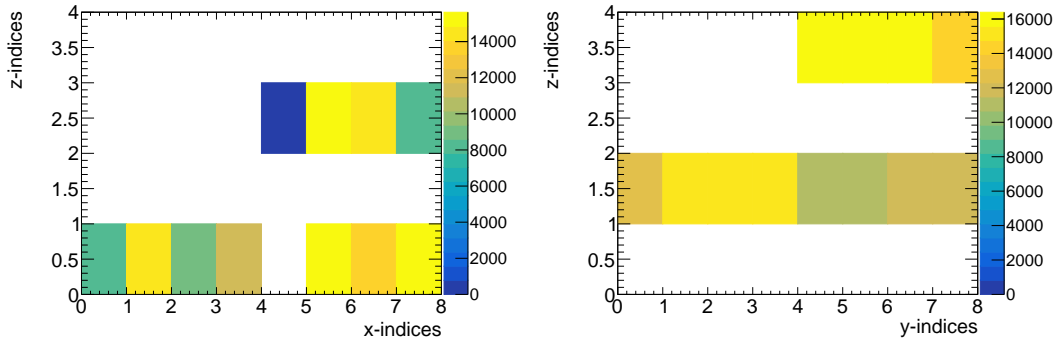
(a) Distribution of the pairs in the x-direction

(b) Distribution of the pairs in the y-direction

Figure 4.10: Distributions of any vertical pair successive hits, requiring that the other fingers of the hodoscope in question should be empty.
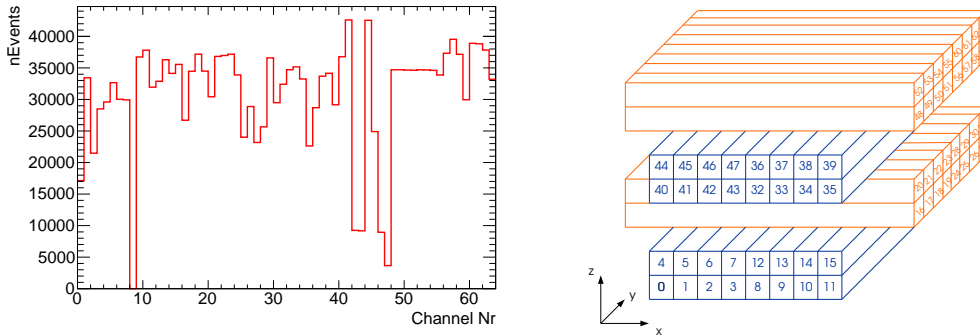

Figure 4.11: The distribution showing how often each channel is hit (left) depicted next to a sketch from the hodoscope pile from Figure 4.2 for clarification.

fluctuations in the channel numbers corresponding to the left upper pack in the x-direction, yet none of these channels are completely defective.

In order to better understand what exactly is happening in this left upper pack, Table 4.1 was constructed. This table shows the number of times a vertical pair of hits was registered in the upper hodoscope (hodoscope number 2) at index j given that a vertical pair of hits was also registered at index i, for any $i, j \in \{0, 1, 2, 3, 4\}$. Apart from the indices corresponding to the upper left pack, index 4 was also added to this table as Figure 4.10a shows a dark blue spot at this index, indicating something might be going wrong here as well.

In this table it can be seen, for example, that practically every time a vertical pair of hits was registered at index 3, indices 0, 1 and 2 also registered a vertical pair of hits. A similar effect is visible when considering index 2: every time a

Table 4.1: Correlated hits vertical pair analysis.

(x, z)	$(0, 2)$	$(1, 2)$	$(2, 2)$	$(3, 2)$	$(4, 2)$
$(0, 2)$	32 761	18 694	8 937	3 653	10 983
$(1, 2)$	18 694	24 883	8 943	3 659	7 736
$(2, 2)$	8 937	8 943	8 943	3 659	538
$(3, 2)$	3 653	3 659	3 659	3 659	538
$(4, 2)$	10 983	7 736	538	538	14 671

vertical pair of hits was registered at index 2, a vertical pair of hits was also registered at indices 0 and 1. It can be concluded that in the upper left pack certain channels will readout a hit whenever an adjacent channel reads out a hit and thus can be considered as defective. This effect now also explains the two asymmetries in Figure 4.9a. Since the upper left pack almost always lights up with multiple hits in the same layer, most of the events which pass through this defective part of the hodoscope pile are vetoed by the requirement that within a layer no more than one cluster of hits containing a maximum of two hits is necessary to perform a decent fit. There are two kind of events that get vetoed by this effect:

1. Those who enter the hodoscope pile with an angle $\theta > 90°$ which, by the requirement of needing to produce a hit in at least three layers, most probably travel through the left upper pack and right bottom pack. Those events would, if they were fittable, also frequently hit the $z = 0$ plane on the right side of the hodoscope pile ($x_0 > 16$). By vetoing these events, there are more roots fitted at the right side of the hodoscope pile than the left side.

2. Those who enter the upper left pack at an angle of $\theta \sim 90°$. Once again, by the requirement that at least three layers need to be hit, vetoing these events leads to vetoing all events entering the left side of the hodoscope pile which results in the asymmetry within the edges of the pile.

This analysis thus explains the reason behind the asymmetries in Figure 4.10a. However, from Table 4.1 the link with index 4 (the dark blue bin) is not that convincing. This is because most events where a vertical pair was readout at index 4 look like the following example:

```
-------- 11110000
-------- 11110000
10001000 --------
01001000 --------
-------- 00000000
-------- 00000000
00010000 --------
00000000 --------
```

A pair of vertical hits in index 4 induces not necessarily a vertical pair in another index, but does often occur together with hits in indices 0 and/or 1. In order to avoid this bias created by the defective part of the hodoscope pile, we choose to solely focus on events going through the right side of the pile according to the requirements laid out in section 4.2.3. The price to be paid here is the decreasing range of angles that can be obtained.

An upside to this situation is that the assumption that all used fingers are in equal distance separated from each other is correct. As briefly discussed in section 4.2.2 it was assumed that all fingers are equally separated from one another in distance, even though it was clear that there is a wider gap between the left and right pack of each hodoscope. Since only the right side will be taken into account, the spacing of the fingers on the left side are irrelevant when linking a position to a hit according to the process laid out in section 4.2.2.

This same analysis was performed for the y-direction, which yielded a similar conclusion. Also here, the problem lies in the upper left pack where, as it turns out, if one of the fingers is hit, often the entire pack lights up. Furthermore, the few externally triggered events for which the hodoscopes were not empty, showed a completely lit up left upper pack. It became clear that in the y-direction the left part of the hodoscope pile should be ignored as well to avoid a bias.

The reason why these parts of the hodoscopes delivered faulty results is not entirely clear. When they were placed on the demonstrator in 2017 they were tested extensively by the milliQan collaboration. It is possible that by detaching them from the demonstrator and placing them on a pile, we scratched some of the tape wrapped around the fingers or damaged parts of the readout.

4.3.3 Analysis Using the Functional Part of the Hodoscope Pile

Now that the defective parts of the hodoscope pile have been identified and removed from the picture, the analysis concerning the angular distributions of the events can be resumed. The resulting distributions can be found in Figure 4.12. Both histograms look much more satisfying in terms of symmetry when compared to Figure 4.7.

It is important to notice that the shape of these distributions is mostly determined by the requirement that at least three layers need te be hit in at least one of the two directions. When a cosmic particle falls in on the used part of the hodoscope pile under an angle of 90°, it will virtually always (depending on the efficiency of the readout) produce a hit in four layers of the considered direction. This cannot be said for particles falling in under an angle of, for example, 60° which will, more often than not, leave a trace in only two of the four layers. This is a direct consequence of the limited width of the used

(a) θ-distribution
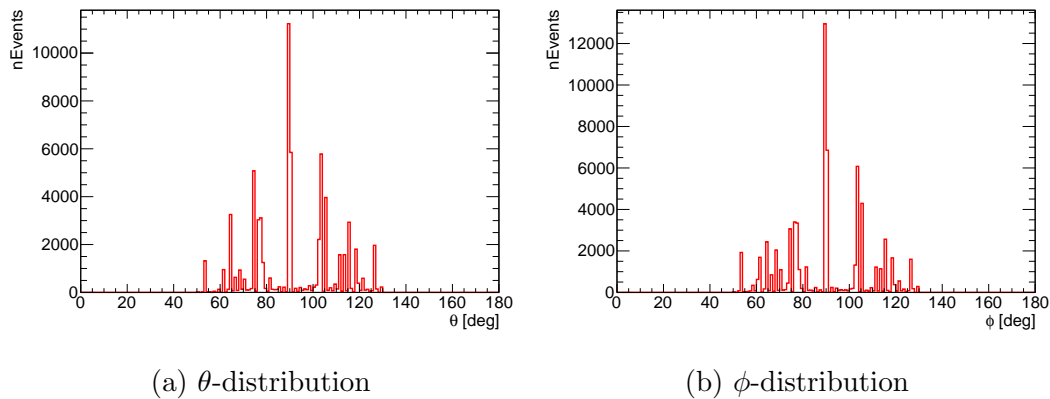
(b) ϕ-distribution

Figure 4.12: Angular distributions, ignoring the left side of the hodoscope pile in both directions.

tracking pile as well as the poor granularity.

Also the distributions of the roots of the fit with the x- and y-axis show much more symmetry when only taking the right side of the hodoscope pile into account, as can be seen in Figure 4.13.

(a) Roots x-axis

(b) Roots y-axis
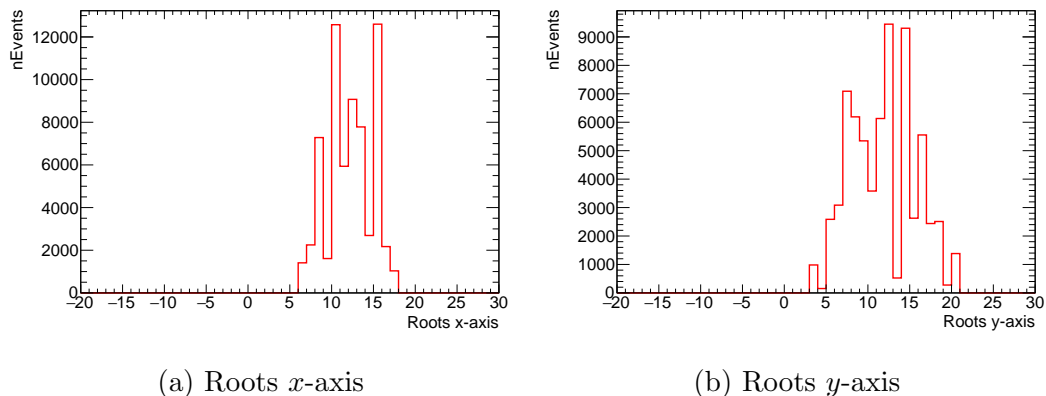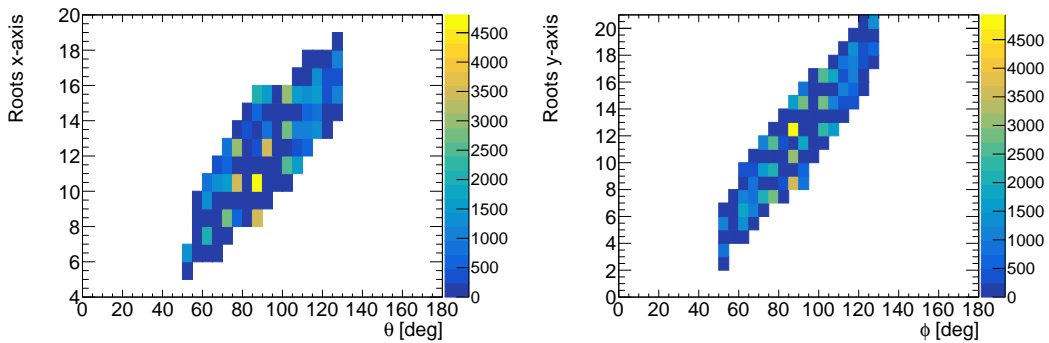
Figure 4.13: Distribution of the points of intersection with the $z = 0$-plane, ignoring the left side of the hodoscope pile in both directions.

Now the edges of the used hodoscope pile are defined by the positions 8 and 16. In the distribution of the roots on the x-axis it can be seen that outside these edges the histogram is almost perfectly symmetric. The distribution of the roots on the y-axis fluctuates a little bit more outside the edges of the pile, which can be attributed to the fact that the bottom layer in the y-direction lies at a vertical position of $z = 5$, which makes the value of the root on the y-axis much more sensitive to the fitted slope than in the x-direction.

Within the edges of the used part of the hodoscope pile, neither of the distributions show the same strong asymmetry as in Figure 4.8. When looking more closely, it can be noticed that these distributions peak at even values. This

may seem rather odd, given the fact that positions with an even number arise only when in the same layer two adjacent fingers are hit, which is expected to happen much less frequently than a single hit in one finger. This effect can be explained by examining the angular distributions in Figure 4.12. It can be seen that the actual peak does not arise at exactly 90° but actually at 89°, which is most probably a result of the finite accuracy on the fitted parameters. Therefore, if, for example, a particle enters the used part of the hodoscope pile in the x-direction at position $x = 10$ under an angle of 90°, it will produce hits in every finger at $x = 10$. It is now very likely that the fitted trajectory will follow an angle of 89°, which would mean that the root of the fit will not be at exactly $x = 10$ but slightly below this value. As a result, this event will be placed in the bin $x = 9$ in Figure 4.13a.

When studying now how the distributions of the roots depend on the angular distributions by placing the events in a two-dimensional histogram as shown in Figure 4.14, it can be seen that not only the shape of the histogram is much more symmetrical than in Figure 4.9, but the events are also more symmetrically distributed. Also the outliers which were visible before removing the left side of the hodoscope pile in both directions are no longer present. The chessboard pattern which can be observed is caused by the same effect which causes the peaks and slumps in Figure 4.13.

(a) 2-D histogram for the x-direction   (b) 2-D histogram for the y-direction

Figure 4.14: Two-dimensional histograms displaying the distributions of the intersection points with the $z = 0$-plane in function of the angular distributions, ignoring the left half of the hodoscope pile in both directions.

4.3.4 Interpretation of the Results

The fact that the angular distributions of cosmic radiation, measured in the drainage gallery, appear to be symmetric is an interesting observation in its own right. This indicates that the two shafts depicted in Figure 2.4a seem to have no significant impact on the distribution of the internal background. This analysis cannot, however, confirm whether the distribution follows a $\cos^2(\theta_{\text{zenith}})$ as

has been measured on the surface of the Earth. Even though the maximum at 90° with the horizontal plane (or, equivalently, at a zenith angle of 0°) with symmetrically decreasing values at both sides of the distribution seems to be consistent with a $\cos^2(\theta_\text{zenith})$, the shape of the found distribution, as explained earlier this chapter, is mainly due to the limited angular range of the hodoscope pile. In order to confirm if, even 70 m underground, the $\cos^2(\theta_\text{zenith})$ distribution holds or how it is shaped by cosmic muon attenuation in the ground above the milliQan cavern, some follow-up studies should be performed using more events, better granularity and simulations using the incoming flux and flux loss.

The effect of positioning milliQan underground can be quantified by estimating the cosmic muon flux in the cavern using the information of the rate a single finger. Here the finger linked to channel 61 was used

$$\Phi_\text{cosmic} = \frac{N_\text{finger 61}}{A_\text{finger}\, t_\text{tot}} \simeq 0.59 \text{ events}\,\text{m}^{-2}\,\text{s}^{-1}\,,$$

where A_finger is the total surface of a single finger, t_tot is the total duration of the run of the hodoscope pile and $N_\text{finger 61}$ is the number of events measured by channel 61 during t_tot. Comparing this estimate to the average muon flux at sea level of 167 muons $\text{m}^{-2}\,\text{s}^{-1}$, it seems as if the ground provides a decent shielding from cosmic muons. However, when considering the muon rate to be 0.2 pb [9] and given the fact that the LHC luminosity peaked in 2018 at a value of 0.02 Hz pb^{-1}, we get

$$f_\text{LHC muons} = 0.02\,\text{Hz}\,\text{pb}^{-1} \cdot 0.2 \text{ muons}\,\text{pb} = 0.004 \text{ muons}\,\text{s}^{-1}\,,$$

measured by bars which are significantly larger than the fingers used in the hodoscope. This shows that cosmic muons are a very important background which will need to be taken into account and that knowing the exact shape of the distribution is relevant when analyzing results taken with the milliQan detector.

Chapter 5

Conclusion

The idea that Dark Matter can be described as being part of a hidden sector has gained prominence over the last decade. By assuming a massless gauge boson A'_μ associated to an Abelian $U(1)'$ extension to the electroweak $SU(2)_L \times U(1)_Y$ gauge symmetry, the production of particles with a non-integer (or fractional) charge is allowed and therefore (by Gell-Mann's totalitarian principle) guaranteed. If such fractionally charged particles exist, they can be used as a portal to experimentally probe this hidden sector, effectively extending the Standard Model. Thus far several constraints have been set on their existence by several collider experiments as well as research concerning the CMB anisotropy. Nevertheless, a large part of the phase space is still left uncovered.

This thesis introduced a new scintillator-based LHC-experiment called milliQan, designed to slice through this so-far uncovered part of the phase space. This experiment would be placed at the PX56 drainage gallery, near the CMS interaction point. Awaiting the funding for the full detector, the milliQan collaboration installed there in 2017 a 1% demonstrator, which was used to take data throughout 2018.

The main goal when analyzing data with such a demonstrator is background rejection. In this thesis we studied two main types of background. On the one hand we studied the internal background, which consists of radiation inside the scintillators which can possibly induce correlated deposits in other adjacent scintillator bars. On the other hand, we studied the external background, which, for the most part, consists of cosmic muon showers.

5.1 Results of the Research

The internal background was studied by performing in situ measurements at the PX56 drainage gallery with two scintillator bars. These measurements consisted of investigating how the time difference between two hits, one in each bar, which seemingly happened at the same time, depends on the distance between

the two bars. It was found that the spread of the time distribution increases with increasing distance, which indicates that a non-negligible amount of the hits are due to secondary radiation rather then being caused by two different cosmic muons simultaneously hitting each one of the two bars. This result was confirmed by analyzing the event rate which not only decreased with distance, but dropped also when placing shielding in between the two bars.

When installing the full milliQan detector, it is thus important to take into account that some form of shielding which would stop some of the secondary radiation is desirable. Also a proper simulation of this effect is required when analyzing data taken by these scintillators.

For the external background, hodoscopes were used to track the trajectories of cosmic muons in the drainage gallery, with the aim to investigate their angular distributions. These distributions were found to be symmetrical, indicating that the two shafts present nearby have no significant impact on this type of background. Even though the symmetrical aspect is consistent with the $\cos^2(\theta_{\mathrm{zenith}})$-distribution cosmic muons follow on the surface of the Earth, from these studies it cannot be claimed that the same distribution holds in the drainage gallery as the shape of the measured distributions is also a result of the poor granularity of the used hodoscopes.

5.2   Outlook and Further Research

The data that was taken by the milliQan demonstrator, has been analyzed by the milliQan collaboration and the exclusion limits at the 95% confidence level are shown in Figure 5.1. It can be seen that the demonstrator on its own can already slice through a new part of the phase space and can even push the limits recently set by the ArgoNeuT experiment [28] (a liquid argon neutrino detector at Fermilab). Given that this concerns only a 1% demonstrator, the full milliQan detector, once installed, is expected to push these limits much further. The background studies performed in this thesis are of relevance when these sensitivities reached with the demonstrator need to be translated to an updated design for the detector.

Even though the results of the performed analyses are unambiguous, we did encounter certain limitations. When studying the internal background, most of the data taking runs did not run long enough to record a significant amount of cosmics, which would have allowed us to perform a comparative study of the Δt-distribution with the hits due to secondary radiation. Redoing these experiments with longer runs, could definitely be interesting. Also conducting these experiments above ground is something that would complete this analysis, but since higher education was subjected to a lockdown to prevent the spread of the COVID-19 virus, this could not take place this semester.

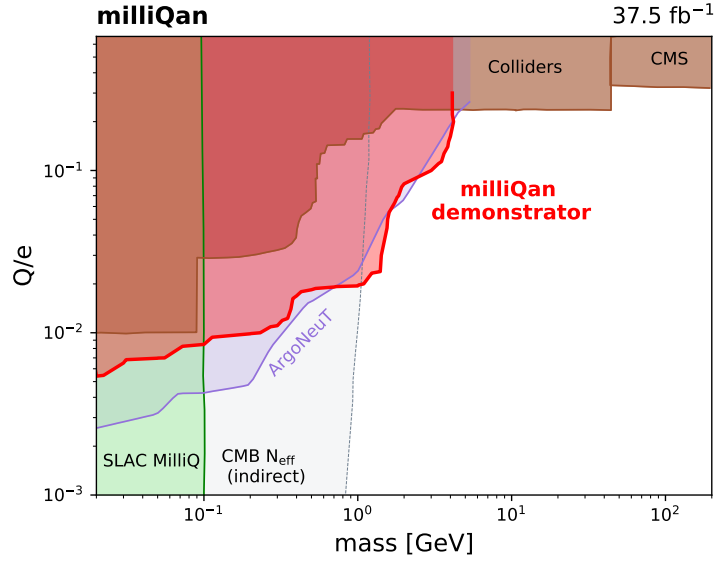The measurements concerning the external background already provided some

Figure 5.1: Exclusion by the milliQan demonstrator at the 95 % confidence level compared to existing constraints from colliders, CMS, ArgoNeuT and SLAC MilliQ [26].

interesting information about the possible impact of the shafts. Nevertheless, also here the experiment should be redone using a tracking device with a higher granularity than the hodoscopes used on the demonstrator in order to confirm (or refute) whether assuming a $\cos^2(\theta_{\text{zenith}})$-distribution is well-founded. As the cosmic muon flux in the drainage gallery is two orders of magnitude larger than the muon rate coming from the CMS IP, knowing the exact shape of this distribution is definitely needed when designing and operating the eventual experiment. These extra studies should be done by applying simulations using information about the incoming flux and flux loss.

Bibliography

[1] Standard model of elementary particles. https://en.wikipedia.org/wiki/Standard_Model. Accessed: February 16, 2020.

[2] F. Mandl and G. Shaw. *Quantum Field Theory.* A Wiley-Interscience publication. Wiley, 2010.

[3] Michael E Peskin and Daniel V Schroeder. *An Introduction to Quantum Field Theory.* Westview, Boulder, CO, 1995. Includes exercises.

[4] Jim Alexander et al. Dark Sectors 2016 Workshop: Community Report. 2016. arXiv 1608.08632 hep-ph.

[5] Paul Langacker. *The Standard Model and Beyond; 2nd ed.* High energy physics, cosmology and gravitation. CRC Press, Jul 2017.

[6] David Vannerom. *Search for new physics in the dark sector with the CMS detector.* PhD thesis, Université Libre de Bruxelles - Vrije Universiteit Brussel, 2019.

[7] Sacha Davidson, Steen Hannestad, and Georg Raffelt. Updated bounds on millicharged particles. *JHEP*, 05:003, 2000.

[8] N. Vinyoles and H. Vogel. Minicharged particles from the sun: a cutting-edge bound. *JCAP*, 2016(03):002–002, 2016.

[9] Steven Lowette. A search for millicharged particles at the lhc. Presentation given at the LHC LLP workshop on November 29th 2019.

[10] Drell–Yan process. https://en.wikipedia.org/wiki/Drell%E2%80%93Yan_process. Accessed: April 8, 2020.

[11] CERN. The Large Hadron Collider. https://home.cern/science/accelerators/large-hadron-collider. Accessed: April 8, 2020.

[12] Large Hadron Collider. https://nl.wikipedia.org/wiki/Large_Hadron_Collider. Accessed: April 8, 2020.

[13] CERN. Linear Accelerator 2. https://home.cern/science/accelerators/linear-accelerator-2. Accessed: April 8, 2020.

[14] CERN. The Proton Synchrotron Booster. https://home.cern/science/accelerators/proton-synchrotron-booster. Accessed: April 8, 2020.

[15] CERN. The Super Proton Synchrotron. https://home.cern/science/accelerators/super-proton-synchrotron. Accessed: April 9, 2020.

[16] CERN. CMS. https://home.cern/science/experiments/cms. Accessed: April 9, 2020.

[17] CERN. LHCb. https://home.cern/science/experiments/lhcb. Accessed: April 8, 2020.

[18] Andrea Latina. Introduction to Transverse Beam Dynamics - Lecture 1: Magnetic Fields and Particle Trajectories, January 2015.

[19] Jorg Wenninger and Michi Hostettler. LHC Report: colliding at an angle. https://home.cern/news/news/accelerators/lhc-report-colliding-angle. Accessed: May 8, 2020.

[20] The CMS Collaboration. CMS Luminosity - Public Results. https://twiki.cern.ch/twiki/bin/view/CMSPublic/LumiPublicResults. Accessed: April 20, 2020.

[21] Steven Lowette. Experimental techniques in particle physics: Lecture 1. Lecture given by Steven Lowette as being part of a master's course "Experimental techniques in particle physics" given at the Vrije Universiteit Brussel.

[22] The milliQan Collaboration. Project Description. Private communication, 2018.

[23] J. Beringer, J. F. Arguin, R. M. Barnett, K. Copic, O. Dahl, et al. Review of particle physics. *Phys. Rev. D*, 86:010001, Jul 2012.

[24] A. A. Prinz, R. Baggs, J. Ballam, S. Ecklund, C. Fertig, et al. Search for millicharged particles at slac. *Physical Review Letters*, 81(6):1175–1178, Aug 1998.

[25] Matthew Citron. Analysis of the milliQan demonstrator data at the LHC. Internal note, 2019.

[26] A. Ball et al. Search for millicharged particles in proton-proton collisions at $\sqrt{s} = 13$ TeV. May 2020. arXiv 2005.06518 hep-ex.

[27] Prashant Shukla and Sundaresh Sankrith. Energy and angular distributions of atmospheric muons at the Earth. *Int. J. Mod. Phys. A*, 33(30):1850175, 2018.

[28] R. Acciarri et al. Improved Limits on Millicharged Particles Using the ArgoNeuT Experiment at Fermilab. *Phys. Rev. Lett.*, 124:131801, 2020.

Acknowledgments

To finalize this thesis, I would like to formally thank some people without whom this thesis in its current form would not have been possible.

Naturally my supervisor prof. dr. Steven Lowette should be mentioned here. Not only did he provide me with a very interesting thesis topic, he has done an amazing job at guiding me through the process. I enjoyed our weekly meetings during which he always succeeded in providing me with more insights which motivated me to further investigate the often odd results I encountered throughout this research.

On that note, I would like to thank the entire milliQan collaboration and, more specifically, prof. dr. David Stuart, dr. Matthew Citron and dr. Brian Francis, who took time out of their busy schedules to guide me through the measurements performed at the drainage gallery at CERN. Being able to work on the detector I was analyzing data with truly gave an extra dimension to the experience of my master's project.

On a more informal note, I thank my friends and classmates Dieder Van den Broeck, Zeb Van Ranst and Sander De Keersmaeker. Even though over the past semester we could not physically support each other, your absurd humor transferred over social media has given me the necessary distraction from my thesis.

Yens Killian Elskens